Ti- and Zr-minerals in calcite-dolomite marbles from the ultrahigh-pressure Kimi Complex, Rhodope mountains, Greece: Implications for the *P-T* evolution based on reaction textures, petrogenetic grids and geothermobarometry

ALEXANDER PROYER[1,*], IOANNIS BAZIOTIS[2], EVRIPIDIS MPOSKOS[3] AND DIETER RHEDE[4]

[1]Department of Earth Sciences, University of Graz, Universitätsplatz 2/II, A-8020 Graz, Austria; email : alexander.proyer@uni-graz.at

[2]Department of Mineralogy, Petrology and Economic Geology, School of Geology, Aristotle University of Thessaloniki, 54124, Thessaloniki, Greece.

[3]Department of Mining and Metallurgical Engineering, Section of Geological Sciences, National Technical University of Athens, Heroon Polytechniou 9, 15780 Athens, Greece.

[4] Deutsches Geoforschungszentrum (GFZ), Section 4.2 Anorganic and Isotope Geochemistry, Telegrafenberg, D-14473, Potsdam, Germany

* present address: Department of Geology, University of Botswana, Private Bag UB 00704, Gaborone, Botswana; email: alexander.proyer@mopipi.ub.bw

ABSTRACT

Rutile, titanite and zircon formed as relatively coarse-grained accessory minerals in several samples of high-grade calcite-dolomite marble with an early ultrahigh-pressure history and decomposed to a texturally complex set of secondary minerals during subsequent stages of retrograde metamorphism. These reactions involve several generations of geikielite-ilmenite as well as zirconolite ($(Ca,Th,U)Zr(Ti,Fe,Nb,Ta)_2O_7$), kassite/cafetite ($CaTi_2O_4(OH)_2$) / $CaTi_2O_5{\cdot}H_2O$), Ti-bearing humite group minerals, thorianite and sometimes euxenite

((Ca,U,Th,REE)(Nb,Ta,Ti)$_2$(O,OH)$_6$). Stable coexistence of zircon and olivine is observed and stably coexisting titanite with olivine and/or humite-group minerals is reported here for the first time outside of carbonatites, kimberlites or lamprophyres. Petrogenetic grids constructed for Ti- and Zr-bearing olivine/antigorite-saturated calcite-dolomite marbles show that geikielite is stable at highest pressures, followed by titanite and rutile, and that baddeleyite + diopside replaces zircon + calcite to higher pressures. The observed reaction textures are consistent with an earlier derived *P-T* path for the Kimi Complex. They corroborate a period of heating during decompression from 25 to 20 kbar and ca. 800 °C, where the assemblage olivine-diopside-spinel-rutile-zircon formed. This assemblage partially re-equilibrated during subsequent decompression and cooling, thus forming the observed reaction textures. Even though no memory of the UHP path is preserved in the accessory minerals, their reaction relationships in general turn out to be potentially very useful for geothermobarometry over a large range of metamorphic conditions.

Keywords: Ti-minerals, zirconolite, kassite, cafetite, impure calcite-dolomite marbles

INTRODUCTION

Zr- and Ti-minerals in carbonate rocks are rarely discussed in the context of regional metamorphism. Their low modal abundance and the fact that reactions amongst them are characterized by very slow reaction rates – rims of ilmenite or titanite around rutile are a very common feature in metabasites or metapelites – makes them very difficult to use for geothermobarometry or the mapping of isograds on a regional scale. A notable exception exists in the field of contact metamorphism: Ferry (1996) mapped isograds of Ti- and Zr-minerals around the Ballachulish contact aureole in Scotland. In a follow-up study, Ferry et al. (2002) calibrated the breakdown of rutile + magnesite to geikielite and of zircon + magnesite to baddeleyite + forsterite experimentally. Fraser et al. (2004) then dated baddeleyite from the Ballachulish aureole to determine the age of the reaction zircon + dolomite = baddeleyite +

55 forsterite + calcite + CO_2. Marble-hosted zircons have been used in several cases for dating
56 (e.g., Liu et al. 2006; Garnier et al. 2006) and for inclusion studies, e.g., for finding ultrahigh-
57 pressure mineral inclusions in zircons from diamond-bearing marbles in Kokchetav
58 (Katayama et al. 2002), but only Ferry and co-workers have yet been using it as an actual
59 participant in metamorphic reactions with other Zr-minerals. Titanite is a typical mineral in
60 regional or contact metamorphic calcite marbles. Rutile is less commonly reported from
61 marbles, but can be found – particularly in those cases where pieces of marble are dissolved in
62 hydrochloric acid and the insoluble residues investigated (e.g., Sastna and Prikryl 2009). The
63 two minerals are related by the reaction
64
65 $$\text{rutile} + \text{calcite} + \text{quartz} = \text{titanite} + CO_2 \qquad (1),$$
66
67 which is valid for calcite-dolomite marbles, too, as long as they are quartz-bearing. Titanite in
68 quartz-free calcite-dolomite marbles is very rare and has not yet been observed coexisting
69 with diopside or even olivine (Dunn 2005). Rutile has been reported as part of the assemblage
70 forsterite + clinochlore + calcite + dolomite + spinel + graphite in a marble xenolith in a
71 diorite pluton (Young and Morrison 1992), but the usual Ti-carrier in a forsterite-bearing
72 marble is humite-group mineral, often Ti-clinohumite (e.g., Franz and Ackermand 1980;
73 Ehlers and Hoinkes 1987, Tropper et al. 2007, etc.)
74 The main focus of this contribution is a description of the reaction textures and products
75 generated by a multi-stage breakdown of Zr-bearing rutile in a calcite-dolomite marbles, the
76 construction of petrogenetic grids for Ti- and Zr-bearing calcite-dolomite marbles to establish
77 a general understanding of stability fields, and geothermobarometry that includes Ti- and Zr-
78 minerals for a more detailed and refined understanding of the metamorphic evolution of these
79 rocks.

Amongst the less common minerals involved are zirconolite, euxenite, geikielite and kassite/cafetite, and the accompanying U/Th-minerals U-pyrochlore and thorianite $(Th,U)O_2$. Out of these, zirconolite has received much attention from applied mineralogists due to its capacity to accommodate and store radioactive elements and is one of the components in "Synroc" ceramics for nuclear waste management (http://www.world-nuclear.org/info/inf58.html).

In natural samples, the Ca-Zr-titanate zirconolite with the ideal formula $CaZrTi_2O_7$ is a relatively rare accessory mineral that has been reported from ultramafic to intermediate Si-undersaturated magmatic rocks including kimberlites and carbonatites, from some high-grade marbles and granulites as well as several lunar samples (e.g., from Apollo 17 sample-norite 78235; Zhang et al. 2012). A detailed review about zirconolite occurrences is given by Gieré et al. (1998) who also summarize the range of compositional variations as follows: The M8 site of Ca can also be occupied by actinides (ACT, mainly U^{4+} and Th^{4+}) and rare earth elements (REE). The M7 site of Zr^{4+} is of course also used by Hf^{4+} and rarely by small amounts of actinides and REE. The M5,6 sites of Ti show a broad range of substitutions by Me^{2+}, Me^{3+} and Me^{5+} ions, and in rare instances also by Zr^{4+} or W^{6+}. $Me^{2+} = Mg^{2+}$, Fe^{2+}, Mn^{2+}, Zn^{2+}; $M^{3+} = Al^{3+}$, Fe^{3+}, Cr^{3+}; $Me^{5+} = Nb^{5+}$, Ta^{5+}. Natural zirconolites can be described by the five endmembers $CaZrTi_2O_7$, $CaZrMe^{5+}Me^{3+}O_7$, $ACTZrTiMe^{2+}O_7$, $REEZrTiMe^{3+}$ and $REEZrMe^{5+}Me^{2+}O_7$. Zirconolites from contact and regional metamorphic metacarbonate rocks have been described by Purtscheller and Tessadri (1985), Gieré (1986, 1989), Williams and Gieré (1988), Kato and Matsubara (1991), Stucki et al. (2001), Nishio and Minakawa (2004), Tropper et al. (2007) and Pascal et al. (2009). According to Gieré et al. (1998), zirconolites from metacarbonate rocks are low in Nb and Ta and can be described by the two main substitutions $ACTMe^{2+}Ca_{-1}Ti_{-1}$ and $REEMe^{3+}Ca_{-1}Ti_{-1}$.

Geikielite (ideally $MgTiO_3$) is the Mg-equivalent of ilmenite with which it forms a complete solid solution series. Hence, members of this series with $X_{Mg} > 0.5$ are called

geikielite, those with $X_{Mg} < 0.5$ are ilmenite. It is a typical mineral for high-grade metamorphic dolomitic marbles and also occurs in carbonatites, kimberlites and serpentinized ultramafic rocks. Significant amounts of Mn (end-member pyrophanite $MnTiO_3$) can also be present.

Kassite (ideal formula $CaTi_2O_4(OH)_2$) and its polymorph cafetite (ideal formula $CaTi_2O_5 \cdot H_2O$) are rare hydrous Ti-minerals which were first described from the Afrikanda pyroxenite massif, Kola peninsula, Russia (Evans et al. 1986, and references therein), where they occur as fillings of miarolithic cavities in alkali pegmatites, apparently as breakdown products of precursors like perovskite, rutile and ilmenite. Mitchell and Chakhmouradian (1998) describe kassite as a replacement product of perovskite in a kimberlite and Popova et al. (1998) and Grey et al. (2003) describe chromian kassite as a secondary mineral from a chromite deposit in the Northern Urals. If the present mineral can be confirmed as kassite or cafetite, it would be to our knowledge the first report of such a mineral from a regional metamorphic marble.

GEOLOGICAL CONTEXT AND SAMPLE PETROGRAPHY

In the Rhodope mountains of northeastern Greece (Fig. 1) microdiamond-bearing gneisses have been reported from the high-grade metamorphic Kimi Complex, indicating a Jurassic ultrahigh-pressure history (Mposkos and Kostopoulos 2001; Perraki et al. 2006; Baziotis et al. 2008; Bauer et al. 2007). The Kimi Complex consists of a variety of rock-types: leucocratic orthogneisses, paragneisses and micaschists, serpentinites, mafic granulites, eclogites and amphibolites as well as marbles with a complex tectonometamorphic history lasting from at least 180 to 65 Ma (Mposkos and Krohe 2006; Bauer et al. 2007, Krenn et al. 2010). The marbles are predominantly white and very pure calcite marbles, but subordinate calcite-dolomite marbles have been found near the village of Organi and were studied with regard to

their metamorphic record by Mposkos et al. (2006) and Proyer et al. (2008). All calcite-dolomite marbles contain additional phlogopite and most of them also olivine and diopside, where olivine replaces a first generation of rarely preserved diopside-1 and is overgrown itself by a thin corona of diopside-2. Spinel and Ti-clinohumite can be present as additional "peak metamorphic" phases whereas slightly aluminous tremolite, chlorite and serpentine have partially or completely replaced the aforementioned minerals during exhumation (Proyer et al. 2008). Zr- and Ti-bearing minerals (other than Ti-clinohumite) were observed in only four of these marble samples.

ANALYTICAL CONDITIONS

The mineral chemical analyses of lower precision level (Table 1) were carried out using a JEOL JSM 6310 high resolution scanning electron microscope with an energy dispersive system (EDS) and wavelength dispersive (WDS) at the Institute of Earth Sciences, Karl-Franzens-University, Graz, Austria. Analytical conditions were: acceleration voltage 15 kV, beam current 6 nA, beam diameter 1-4μm and time for data acquisition 100 sec. Na, F analyses were obtained using the WDS system with counting times of 20 seconds on the peak and 10 seconds on the lower and upper background. Mineral standards, used for the normalization of the elements were: calcite (Ca), magnesite (Mg), siderite (Fe) and rodochrosite (Mn) for the carbonates, garnet (Mg, Fe), corundum (Al), quartz (Si), adularia (K), titanite (Ca, Ti), rhodonite (Mn), jadeite (Na) and F-phlogopite (F) for the silicates and oxides. The 1σ standard deviations range between 0.08 wt% for transition elements to 0.16 wt% for Si and Al, and 0.28 wt% for Mg (all EDX) and 0.06 for Na (WDX) for high concentrations and are always less than 1.5 % of the analysed value.

Additional electron-microprobe analyses of samples were performed in the wavelength-dispersive mode using the JEOL JXA-8500F (Hyperprobe) at the Deutsches GeoForschungsZentrum in Potsdam, Germany. Operating conditions involved an accelerating

158 voltage of 15 or 20 kV, a beam current of 20 - 40 nA and a beam diameter of 1 μm. Kα-lines
159 were used for Na, Mg, Al, Si, P, K, Ca, Ti, Mn and Fe; Lα-lines for Y, Sr, Zr, Nb, La, Ce, Yb,
160 Lu, Ta and W; Lβ-lines for Pr, Nd, Sm, Gd, Dy, Ho, Hf; Mα-line for Th and Mβ-lines for Pb
161 and U. The counting times on the peaks were 20 - 100 s for the elements and, in each case
162 halftime for background counts on both sides of the peak. X-ray lines and background offsets
163 were selected so to minimise interference between elements during analysis. Standards for
164 calibration were well-characterised natural and synthetic materials including albite (Na),
165 periclase (Mg), corundum (Al), zircon (Si, Zr), orthoclase (K), wollastonite (Ca), rutile (Ti),
166 rhodonite (Mn), hematite (Fe), strontianite (Sr), REE-phosphates (P, Y, La, Ce, Pr, Nd, Sm,
167 Gd, Dy, Ho, Yb and Lu), HfO_2 (Hf), vanadinite (Pb) and metals (Nb, Ta, W, U and Th). The
168 matrix corrections were employed according to the Armstrong-CITZAF method (Armstrong
169 1995). Average 1σ standard deviations for each element are given in the last column of Table
170 2 and range between 40 and 580 ppm.
171
172 **SAMPLE PETROGRAPHY**
173 **Sample 4RA28** is almost un-retrogressed, with fresh olivine, diopside (individual grains
174 and rims around olivine), amphibole and chlorite (Fig. 2a). Accessories are apatite and zircon,
175 which occurs as inclusions in olivine and dolomite, but also in the matrix (Figs. 2b-e). It
176 forms un-corroded, rounded grains with minor compositional zoning (Figs. 2c-e), and often
177 contains inclusions of U-Th-oxides (qualitatively determined from EDX spectra). The latter
178 occur also separately in the matrix and might have served as nuclei for zircon growth.
179 **Sample 5K3a** is a strongly retrogressed calcite-dolomite marble with antigorite, chlorite,
180 phlogopite and talc as the main silicate phases. Olivine, diopside and Ti-bearing humite group
181 minerals have been found as sometimes well preserved relics, but no amphibole. Olivine is
182 intergrown with or overgrown by diopside and Ti-humite (Fig. 3a). Diopside has rare
183 inclusions of Mg-poor calcite (Fig. 3b), is sometimes intergrown with Ti-clinohumite and

replaced at a late stage by serpentine and calcite. Titanite is relatively coarse-grained and occurs as numerous well preserved rounded inclusions in calcite and dolomite (Fig. 3c) but also in intergranular space where it can show various degrees of corrosion and replacement. An early type of replacement is overgrowth by Ti-bearing humite group mineral, which is chondrodite in Figure 3d. This would indicate that titanite may well have coexisted once with olivine and the other early silicate minerals. Later-stage replacement of titanite is characterized by fine-grained rutile + calcite ± serpentine (Fig. 3c) or rutile + geikielite + serpentine (Fig. 3e). Serpentine-rutile intergrowths are very common and characteristic – rutile is always extremely fine-grained in such a case – and could be pseudomorphs after a former Ti-bearing mineral of the humite group. Figure 3f shows such a possible pseudomorph which contains additional dolomite with a titanite inclusion in its core.

Fresh zircons were found as inclusions in phlogopite; another single grain shows development of a reaction rim of Th-zirconolite (Fig. 3g); in most cases zircon forms larger grain aggregates or skeletal grains intergrown with zirconolite, thorianite and rare euxenite (Figs. 3h,i). One titanite inclusion in calcite is accompanied by Th-bearing zirconolite (Fig. 3j). Zirconolite single crystals are rare, idiomorphic to xenomorphic, with the most prominent zonation in Th-content (Fig. 3k) and sometimes enrichment of U along some rim portions, as well as marginal growth of euxenite.

Sample 5K6a: Two thin sections were cut from this sample. **5K6a-1** is a strongly retrogressed calcite-dolomite marble with serpentine, chlorite, amphibole and spinel as the main additional constituents. No olivine or diopside is preserved, as in the other samples. Rutile is observed both as a matrix phase and as an inclusion in spinel (Fig 4a). Whereas rutile entirely included in spinel is “fresh” and even a rutile grain found in serpentine (former olivine) is completely unaltered, one rutile grain formerly included in spinel and now in contact with the matrix shows minor transformation into geikielite (Fig. 4b). In the matrix,

rutile is invariably overgrown and replaced by a first generation of geikielite (geikielite-1, Figs. 4c-f).

Texturally, there seem to be three different types of geikielite (Fig. 4c): Geikielite-1 directly replaces rutile and sometimes hosts inclusions of a first generation of zirconolite (zirconolite-1, Th-poor). Geikielite-2 is medium-grained and intergrown with chlorite and sometimes subordinate amounts of additional phlogopite, calcite and serpentine (Fig. 4c, top right). Geikielite-3 has quite variable BSE contrast, a very fine-grained, "spongy" texture and is intergrown with equally fine-grained serpentine (Fig. 4c, bottom). In some instances, titanite is observed in a grain size similar to rutile and geikielite1, always adjacent to and intergrown with the former two minerals (Figs. 4e,f) but invariably corroded and replaced by geikielite-3.

Chemically homogenous geikielite-1 with or without small inclusions of rutile or zirconolite is the most common Ti-accessory in this sample. Geikielite-2 is similar in composition to geikielite-1 but occupies a clearly distinct textural position at the margin of rutile-geikielite-1±titanite cores and sometimes develops Th-enriched zirconolite-2 at its rim (Table 1). Rare thorianite was also found in the geikielite-2 domain. Geikielite-3 varies in composition from BSE-darker geikielite to BSE-brighter ilmenite and forms a very delicate, spongy, symplectite-type structure within or next to geikielite-2 intergrowths (Figs. 4a, c), thus more or less enveloping parts of or even the entire inner core of rutile-geikielite-1-titanite relics. Geikielite-3 is generally rather Mg-rich around titanite relics (Figs. 4 e,f,g) and Fe-rich in other domains. It often appears to be pseudomorphic and can even be part of symplectitic coronas around such pseudomorphs (Fig. 4h). The distribution of Mg-rich and Fe-rich varieties in pseudomorphs is uneven (Fig. 4i), which invites more than one explanation for their genesis.

The pseudomorphs and coronae can also get very complex in mineralogical composition: the most common constituents additional to geikielite are calcite, serpentine, retrograde rutile-

2 and a Ca-Ti-compound with an analytical total of ca. 90 wt%, tentatively classified as kassite or cafetite (Fig. 4j). Less common constituents are zirconolite and titanite. In terms of geikielite evolution, it is interesting that geikielite-1 often forms separate grains in the matrix, with or without a rim of geikielite-3 (Fig. 4j). Geikielite-2 usually develops towards a chlorite matrix (Fig. 4l,m). In rare cases titanite appears in the same textural habit as geikielite-2 (Fig. 4m), almost indistinguishable in BSE-grey scale intensity.

5K6a-2 is another section cut from the same sample and also contains calcite, dolomite, diopside, olivine (partly or completely replaced by serpentine), spinel, amphibole, phlogopite and chlorite. Diopside occasionally forms rims around olivine (Fig. 5a) whereas amphibole coexists with and partly overgrows diopside in turn. Occasionally, it contains numerous sub-idiomorphic inclusions of rutile, perhaps pseudomorphing a former Ti-bearing humite-group mineral (Fig. 5b). The main accessory phases, though scarce, are zircon and titanite. The latter often contains inclusions of rutile and zirconolite (Fig. 5c,d) and is often preserved fresh in a coarse-grained carbonate-chlorite-phlogopite-serpentine matrix. In other cases it is partially corroded at the rim by spongy geikielite -3 and some additional ilmenite, in other places by the typical combination kassite/cafetite + serpentine (Figs. 5c,d,f). Geikielite-1 was observed once intergrown with rutile as an inclusion in titanite (Fig. 5e). Rutile growth in that site, however, may at least partly be secondary from titanite, together with serpentine and calcite.

Sample 5K6b was collected in close vicinity to 5K6a and also contains relics of olivine, diopside, spinel, amphibole and phlogopite in addition to retrograde serpentine and chlorite. Diopside also forms rims around olivine whereas amphibole forms small grains at diopside-olivine interfaces or large blasts in the matrix containing relics of diopside. Fresh rutile in contact with amphibole, dolomite and serpentine (former olivine) indicates that rutile was stable with amphibole, i.e. the transitions observed in the Ti-minerals postdate amphibole growth. Titanite forms single grains or overgrowths on rutile, which occasionally also contain Th-zirconolite (Fig. 6a). Most titanite grains are slightly corroded by spongy ilmenite-

geikielite of type-3 (Fig. 6b) or by late kassite/cafetite + serpentine (Fig. 6c). Geikielite of type-1 was observed once intergrown with rutile next to titanite (Fig. 6c). Medium-sized intergrowths reminiscent of geikielite type-2 consist of rutile (Rt-2) which seems to replace titanite in a reaction texture corresponding to titanite = rutile + calcite (Fig. 6d).

MINERAL COMPOSITIONS

Representative analyses of most minerals are given in Table 1. Zirconolite as well as a few spots on other accessories like rutile, geikielite, euxenite and thorianite were analysed for a large spectrum of elements – these data are shown in Table 2.

Clinopyroxene was observed in all samples except 5K6a-1 and is always diopside. Its composition can range from pure to slightly aluminous (up to 2.3 wt% Al_2O_3 or 0.5 a.p.f.u. Tschermak-component) in these cases the diopside is also titanoan, with up to 0.7 wt% TiO_2. All diopsides contain very minor amounts of FeO (<0.4 wt%), with the exception of sample 4RA28, where diopside has up to 1.4 wt% FeO. The X_{Mg} is 0.99 and 0.96 respectively. Sodium is rarely above detection limit and always less than 0.1 wt% Na_2O.

Olivine was found in the diopside-bearing samples and is very constant in composition throughout: Ni- and Ca-contents are below detection limit, the X_{Mg} is consistently 0.98; only 4RA28 olivines are more ferrous with X_{Mg} of 0.88.

Almost none of the analyses of humite-group minerals yield a cation ratio that fits one of the defined endmembers nicely, so we think that the periodicity of hydrous layers is variable (cf. Ribbe 1982). The analyses listed in Table 1 reflect this situation, and they were labelled clinohumite, humite or chondrodite according to the most closely corresponding cation ratio. The Ti-content ranges between 2.8 and 7.8 wt%. The F-content correlates positively with Ti-content and ranges from 0.87 to 1.27 wt%.

Spinel in thin sections 5K6 is chemically homogenous, with Mn and Zn generally below detection limit. Fe-content is also low (0.02-0.04 a.p.f.u.), and according to formula recalculation mainly in the ferric state.

Amphiboles in sample 4RA28 are tremolite, those in the other samples are calcic and highly aluminous (pargasite), with significant amounts of K (0.50 – 1.34 wt% K_2O or 0.09 – 0.25 a.p.f.u.) and Ti (0.61 – 1.24 wt% TiO_2 or 0.06 – 0.13 a.p.f.u.). F-content ranges from 0.50 to 0.66 wt% or 0.22 to 0.29 a.p.f.u.

Both chlorite and phlogopite are almost pure Mg-endmembers (X_{Mg} = 0.98-0.99) and Al-poor (Al = 2.18-2.34 a.p.f.u. in chlorite and 1.10 – 1.40 a.p.f.u. in phlogopite). Ti-content of phlogopites are significant (0.60-0.70 wt% TiO_2 or 0.03 a.p.f.u.), F ranges from below detection limit to ca. 0.9 wt% or 0.20 a.p.f.u., i.e. an X_F of 0.10). Only chlorite in sample 4RA28 is again a bit more ferrous, with X_{Mg} = 0.93.

No compositional zoning is visible in titanite even at high-contrast BSE imaging. However, Al-content varies slightly between grains from 1.4 – 2.0 wt% Al_2O_3, which corresponds to 0.05 – 0.08 a.p.f.u. This goes along with slightly lower F-contents of 0.02-0.05 a.p.f.u.

Rutile occurs in samples 5K6a and 5K6-3 but was analysed in detail only in the former sample, where the large grains (Rt-1) contain significant amounts of FeO (≤ 0.44 wt%), MgO (≤ 0.74 wt%), SiO_2 (≤ 0.28 wt%) and ZrO_2 (≤ 0.29 wt%), as well as minor Al_2O_3 (≤ 0.09 wt%), CaO (≤ 0.16 wt%), Nb_2O_5 (≤ 0.05 wt%), Ta_2O_5 (≤ 0.14 wt%) and some REE.

Geikielite-ilmenite: Type-1 and type-2 geikielites are chemically indistinguishable. The grain-to-grain variation in composition within one thin section, however, can be significant: X_{Mg} ranges from 0.89 (Fig 1b) to typical values of 0.85 to 0.83 in some rutile-free grains in the matrix. Ilmentite occurs as type-3 and also along late cracks in type-1 grains with an X_{Mg} of 0.15-0.30 and significant amounts on manganese (X_{Mn} up to 0.05 or 2.4 wt% MnO or up to 0.05 a.p.f.u.).

311 The identification of kassite/cafetite is tentative, based only on the microprobe analysis of
312 a Ca-Ti-compound with a Ca:Ti ratio of exactly 0.5 and low analytical totals of around 90
313 wt%, which points to a hydrous Ca-Ti-oxide, that could be kassite $Ca[Ti_2O_4(OH)_2]$ or its
314 polymorph cafetite $Ca[Ti_2O_5](H_2O)$ (Krivovichev et al. 2003, Grey et al. 2003). These two
315 minerals can only be distinguished by their structure, which we did not attempt in this study.
316 Mg, Si and F have occasionally been measured slightly above detection limit, but this could
317 also be due to beam overlap because of the small grain size. A slight spread of the electron
318 beam was necessary in order to avoid beam damage. A Raman spectrum of the grain shown in
319 Fig. 5d has been obtained with a red laser (785 nm) and is shown in Figure 7. After
320 eliminating peaks for adjacent minerals like titanite (Fig 7, red line), carbonates and
321 serpentine, the remaining Raman bands are at 283, 372, 396, 451, 677 and 707 wavenumbers.
322 However, there is no good match with any of the rare published spectra of kassite or cafetite
323 (e.g., RRUFF database), so the true nature of this mineral remains ambiguous.
324 The analyses of zirconolite from samples 5K3a and 5K6a-1cluster close to end-member
325 composition in the Zr-Ca-Ti triangle, with slight deviations towards the Zr-apex (Fig. 8a). A
326 close-up shows that 5K3 is more strongly displaced, indicating a higher degree of substitution
327 on the Ca- and Ti-sites (Fig. 8b). The reason for this displacement is mainly the substitution
328 of divalent cations (M^{2+}) together with Actinides (ACT) - viz Figures 8c, d. The amount of
329 REE is generally low and less important than actinides or pentavalent cations (Fig. 9a). REE
330 in 5K3 zirconolites are lower (mostly < 0.015 a.p.f.u.) compared to 5K6, but generally too
331 low to find a definite substitution correlation relationship (Fig. 9b). The contents of M^{5+}
332 cations are slightly higher than REE, but they also show no clear correlation with any of the
333 other components, the best "fit" is a poorly defined positive correlation with Fe_{tot} (Fig. 9c).
334 There seems to be a significant deficiency of Zr + Hf in the M7 site, however there is no
335 correlation between Zr and ACT, REE or Ti, the three possible substitution candidates
336 according to Gieré et al. (1998). The Ti versus Al diagram (Fig. 9d) shows a contrasting

337 correlation for the two samples, with an uncertain positive slope for 5K3 and a clearer
338 negative one for 5K6.

339 Euxenite was detected as very tiny (up to a few micrometers in diameter) intergrowth with
340 zircon, zirconolite and thorianite (Figs. 3h) and contains ca. 10 wt% Nb_2O_5, 3-6 wt% Ta_2O_5,
341 26-28 wt% UO_2 and 3-3.5 wt% ThO_2 (Table 2)

342 Thorianite grains cover two composition ranges. One is almost pure ThO_2 (with up to ~6
343 wt% UO_2) and the other contains around to 20-25 wt% UO_2. The content of other elements is
344 generally low and most likely due to beam overlap with matrix minerals, as the grain size of
345 thorianite is usually also only a few micrometers.

346

347 **METAMORPHIC EVOLUTION OF Ti- AND Zr-MINERALS:**

348 Sample 4RA28 is an olivine-diopside-amphbole-chlorite-marble; it contains no Ti-
349 minerals, and zircon is the only Zr-mineral. U-Th-oxide occurs both as inclusions in zircon
350 and in the matrix, which means that it rather served as a nucleation site for zircon than being a
351 decomposition product of a Zr- and actinide-bearing precursor mineral. The most important
352 aspect of this sample is that zircon can definitely coexist stably with olivine, which is very
353 uncommon for regional metamorphic marbles (but see Ferry, 1996). It not only occurs in the
354 intergranular space of the sample, in the vicinity of fresh olivine and diopside, but also as
355 rounded, uncorroded inclusion in olivine itself.

356 Sample 5K3 is an olivine-diopside-Ti-humite-chlorite-marble with zircon in granular to
357 skeletal growth habits, intergrown with or overgrown by zirconolite. Other less common
358 minerals intergrown with zircon are thorianite and euxenite. Zirconolite also occurs with
359 idiomorphic growth habits and may have been coexisting with and partly replacing earlier
360 zircon.

361 The textures of Ti-minerals indicate a growth sequence of titanite -> Ti-humite -> rutile.
362 Titanite is interpreted to have coexisted once with olivine, which is another very uncommon

363 feature. It is obviously directly replaced by a Ti-bearing mineral of the humite group.
364 Different compositions have been measured for the latter, which may be due to variable
365 small-scale intergrowth of different humite-group minerals. These Ti-carriers are replaced
366 during serpentinization of the rock by a fine-grained intergrowth of serpentine + rutile,
367 sometimes with additional dolomite; in one such instance, a titanite relict was still preserved
368 in the core of such a pseudomorph (Fig. 3f).
369 Despite the great variety of textures observed in the different slices taken from sample
370 5K6, they have the same "peak metamorphic" mineral assemblage in common: olivine +
371 diopside + spinel + phlogopite + rutile + amphibole. Even though there is a textural age
372 sequence of olivine -> diopside -> amphibole, all these minerals are considered to have
373 coexisted stably at one point – still before the onset of reactions responsible for the multi-
374 stage decomposition of Ti-minerals. According to textural criteria the oldest Ti-mineral is
375 rutile (Rt-1), which is slightly Zr-bearing and perhaps of detrital or early metamorphic origin.
376 A reasonable genetic explanation of Ti-mineral textures may be as follows:
377
378 **Stage 1**
379 Rutile breaks down to geikielite (type-1 and -2) + chlorite, which indicates that the
380 reaction also involves breakdown of spinel. Such a reaction would be:
381
382 $$\text{spinel} + 2\ \text{rutile} + 3\ \text{olivine} + 4\ H_2O = 2\ \text{geikielite} + \text{clinochlore} \quad (2)$$
383
384 Whereas geikielite-1 pseudomorphically replaces rutile, geikielite-2 grows towards the
385 matrix, very often towards (former) spinel sites, as indicated by intergrown chlorite. Being
386 compositionally identical, these two textural types most likely developed at the same time.
387 Th-poor zirconolite included in geikielite-1 is preserved from later alteration phenomena,
388 which might have caused a change to more Th-rich compositions (stabilizing effect by passive

389 enrichment) in the matrix-exposed zirconolites associated with geikielite-2. Reaction (2)
390 requires external hydration and was perhaps triggered metastably at the time of fluid
391 infiltration. Where fluid or spinel was scarce or missing near a rutile site, this reaction would
392 only occur partially or not at all.
393
394 **Stage 2**
395 Thin sections 5K6a-2 and 5K6b demonstrate that an alternative transformation of rutile to
396 titanite must have occurred in many cases, possibly by the reactions
397 $$4\ \text{rutile} + 3\ \text{diopside} + \text{dolomite} = 2\ \text{olivine} + 4\ \text{titanite} + 2\ CO_2 \quad (3)$$
398 or perhaps rather
399 $$\text{rutile} + \text{olivine} + 3\ \text{calcite} + CO_2 = \text{titanite} + 2\ \text{dolomite} \quad (4)$$
400 as there is no indication of a late olivine generation.
401 In a disequilibrium (reaction overstepping) situation, these reactions might include
402 geikielite of type-1 or type-2 as an additional reactant. There is rare textural evidence that
403 titanite actually replaced geikielite-2 (Fig. 4m) and was later replaced in these sites by rutile-2
404 + calcite (Fig. 6d). This texture and the fact that the earliest replacement of rutile seems to be
405 by geikielite (Fig. 4b) establish titanite growth as stage 2. But as any of the reactions (2) and
406 (4) strongly depend on the presence of some fluid as a reaction participant, significant
407 amounts of overstepping and even omission of reactions is possible in different parts of the
408 marbles.
409 Both geikielite-1 and titanite grew directly from rutile and may carry zirconolite-
410 inclusions, that accomodated the Zr, Nb and Ta released from rutile. As zirconolite has a
411 significant capacity for the uptake of actinides, it may have removed both U and Th from the
412 pore fluid or may have nucleated on and partly resorbed pre-existing U-Th-oxides.
413
414 **Stage 3**

Late stage textures are generally fine-grained: spongy ilmenite or geikielite of type-3 are intergrown with late, fine-grained serpentine and form simple to multiply complex overgrowth patterns. As both rutile-geikielite-1 intergrowths and single geikielite-1 grains (Fig. 4k) are rimmed by spongy or symplectite-type geikielite-3, and one would not expect geikielite to be replaced by another generation of geikielite of almost the same composition, we conclude that type-3 intergrowths of geikielite-ilmenite have replaced former titanite. Based on the partial replacement of titanite by either geikielite-3 or kassite + serpentine + calcite in 5K6a-2 and 5K6b, we conclude that this type of replacement is almost complete in thin section 5K6a, which would corroborate the above interpretation of essentially all fine-grained type-3 textures as pseudomorphs after former titanite, following a reaction like:

4 titanite + 10 dolomite + 4 H_2O = 4 geikielite + antigorite + 14 calcite + 6 CO_2 (5-1).

The alternative breakdown reactions of titanite to kassite + serpentine and even of titanite to rutile + calcite are often observed in the same location and could be accomplished by very similar model reactions:

4 titanite + 6 dolomite + 4 H_2O = 4 kassite + antigorite + 6 calcite + 6 CO_2 (5-2),

and

4 titanite + 6 dolomite + 4 H_2O = 4 rutile + antigorite + 10 calcite + 2 CO_2 (5-3).

It is not clear what causes these alternative mechanisms. Desilicification due to transformation of olivine and spinel relics to the more Si-rich antigorite and chlorite, however, could be the main cause for the breakdown of titanite to Si-free Ti-minerals.

The complex intergrowth textures of Zr-minerals in sample 5K3 are interpreted as the result of a continuous replacement of zirconolite by zircon, thorianite and euxenite according to the reaction:

441 $(Ca,Th,U)Zr(Ti,Fe,Nb,Ta)_2O_7 + CaCO_3 = ZrSiO_4 + ThO_2 + (Ca,U,Th)_2(Ti, Nb,Ta)_2O_7$ (6),

442

443 during which Th, U, Nb, Ta etc are enriched in zirconolite, thus stabilizing it. This equation is
444 not exactly mass-balanced. U, Nb and Ta are strongly enriched in euxenite compared to
445 zirconolite whereas Zr and most of the Th are released as zircon and thorianite respectively.
446 A more complex reaction history, perhaps involving an early generation of zircon (Zr-1) is
447 indicated by the overgrowth of zirconolite on zircon (Fig. 3g). The zircons in sample 4RA28
448 would as well rather belong to such a first generation.

449

450 **PETROGENETIC GRIDS**

451 A thermodynamic analysis of phase relationships in the system TiO_2- ZrO_2-CaO-MgO-Al_2O_3-
452 SiO_2-CO_2-H_2O (TZCMASCH) has been attempted in order to understand the stability fields
453 of Ti- and Zr-minerals in ultrabasic (olivine/antigorite-dominated) calcite-dolomite marbles.
454 The petrogenetic grid for Ti-bearing marbles in Figure 10 shows the most important stable
455 reactions involving the endmembers forsterite, antigorite, diopside, tremolite, calcite,
456 dolomite, spinel, clinochlore, rutile, geikielite, titanite and H_2O-CO_2 fluid. Stable reactions
457 were found using the software PERPLEX (Connolly 1990, 2005), and the full grid was
458 subsequently developed with the software THERMOCALC version 3.30 (Powell et al. 1998)
459 and the ds55 dataset; (Holland and Powell 1998, and unpublished updates). For the purpose
460 of reducing complexity and making the grid applicable to the most common bulk rock
461 compositions, the carbonates as well as forsterite or antigorite were considered to be in excess
462 and one Ca-Mg silicate (diopside or tremolite) as well. No reactions with three coexisting Ti-
463 minerals are shown. The most important reactions for high-temperature marbles (with spinel
464 as the stable Al-buffer mineral) are grouped around invariant point 1 (IP1) at 19.7 kbar,
465 803°C. They show that geikielite is stable mainly at high pressures, followed by titanite in an
466 intermediate stability field and then rutile at the lowest pressures at temperatures below IP1.

The temperature range below 500°C is dominated by titanite, which is replaced by rutile at relatively low pressures. The activities of titanite and tremolite control this strongly pressure-dependent transition. All reactions around IP1 are fluid-absent, or, in other words, fluid-independent. Therefore fluid composition, which is often an unknown variable in geothermobarometry with marbles, is not an issue. Moreover, the reactions shift considerably in pressure and temperature depending on the endmember activities, which makes them highly suitable for geothermobarometry to the degree that activity-composition relationships (activity models) are well known. Figure 11 illustrates how IP1 shifts if the activity of one endmember is changed (along the reaction where this endmember is absent). The effect is strongest for titanite and still considerable for the other endmembers. Figure 12 shows the petrogenetic grid for Zr-minerals (zircon and baddeleyite) for olivine/serpentine-dominated calcite-dolomite marbles. Due to the lack of thermodynamic data and an activity-composition model for zirconolite, this mineral could not be included in the present analysis. At temperatures above antigorite stability, the assemblage diopside + baddeleyite is stable at elevated pressures whereas zircon + forsterite covers the lower pressure region, indicating the value of this equilibrium as a useful geothermobarometer.

GEOTHERMOBAROMETRY

Figure 13 combines the two grids with the results of geothermobarometry and also shows a *P-T* path derived in a prior study of impure marbles from the same field area (Proyer et al. 2008). The activities derived from measured mineral compositions in sample 5K6a2 were used to calculate *P-T* conditions of equilibration of the assemblage olivine-chlorite-spinel-geikielite-carbonates-fluid (using THERMOCALC in average-*PT* mode, Powell and Holland 1994), as shown by a red ellipse in Figure 13. The calculated *P-T* conditions converge to a minimum 2σ standard deviation (sigfit 0.60) around an X_{CO2} of 0.10 – 0.15 at 763 ± 28°C and 9.2 ± 2.0 kbar. Average-*PT* values derived for sample 5K6b are almost identical (776 ± 24°C

493 and 10.5 ± 2.4 kbar at an X_{CO2} of 0.20). The conditions derived from these two samples are
494 inferred to reflect the main conditions of re-equilibration when geikielite formed
495 contemporaneous with the hydration of spinel to form chlorite (reaction 2). It was concluded
496 from the relatively coarse grained reaction texture that this reaction, even though triggered by
497 external hydration, occurred near equilibrium. The close proximity of the red ellipse to the
498 chlorite-in curve corroborates this conclusion.
499 *P-T* conditions for the peak reaction assemblage olivine-clinopyroxene-titanite-chlorite-
500 titanoan (clino)humite in sample 5K3a are difficult to assess because there is no
501 thermodynamic data for Ti-clinohumite and the humite-group minerals analysed in this study
502 are not well crystallized members of the series but rather disordered crystals with changes in
503 the stacking sequence of the hydrous layers on a micro- to nanoscale. Using measured mineral
504 compositions of olivine, clinopyroxene and chlorite at an X_{CO2} of 0.1 and taking the activity
505 of clinohumite as a variable in average-*PT* calculations shows that the best estimates within
506 the confidence limit converge around an activity for clinohumite (a_{chu}) of 0.07 and 750 ±32°C,
507 9.2 ±1.6 kbar (lower green ellipse in Fig. 13). Variation of X_{CO2} shows that the minimum for
508 optimum fit (sigfit = 0,72) lies between 0.02 and 0.10 X_{CO2}, and the corresponding *P-T*
509 conditions range up to 782 ±30 °C and 15.6 ±1.8 kbar (a_{chu} = 0.15) for the lower X_{CO2} (upper
510 green ellipse in Fig. 13). As the main stage of recrystallization in both 5K6a,b and 5K3a are
511 the result of external hydration, both rocks may have reequilibrated at the same time and
512 under very similar *P-T-*X_{CO2} conditions. No statistically significant *P-T* results could be
513 obtained for sample 4RA28 due to disequilibrium chlorite composition revealed by the
514 average-*PT* statistical diagnostics.
515 Whereas zircon occurs as an accessory mineral in samples 4RA28, 5K3a and 5K6a-2,
516 baddeleyite was not observed in any of the samples. As zircon and baddeleyite are usually
517 close to their endmember composition – the main substitution being Hf for Zr – the actual
518 position of the reaction curve depends on the activities of the other silicates and carbonates

519 involved. The dashed blue curve in Figure 13 was calculated for measured olivine and
520 clinopyroxene compositions in sample 4RA28. Both blue curves are consistent with
521 equilibration of 4RA28 at peak conditions similar to those recorded by samples 5K6a and
522 5K3a, where zircon is also part of the equilibrium assemblage.
523 The *P-T* path derived by Proyer et al. (2008) is largely but not entirely consistent with the
524 information derived in this study. Following that path during exhumation, the assemblage
525 would have evolved during the heating episode in the subducted and overthickenedlower crust
526 (between 25 and 20 kbar) from an olivine-diopside-chlorite-geikielite-baddeleyite-bearing
527 rock to an olivine-diopside-rutile-spinel-zircon-bearing marble – the assemblage that was
528 identified here as the oldest preserved (peak) assemblage. Partial re-equilibration occurred
529 during re-entrance into the chlorite stability field by hydration close to the equilibrium curve.
530 Variable availability of fluorine has partially expanded the stability fields of titanite and
531 titanoan clinohumite, so both minerals became stable at some section of the P-T path instead
532 of geikielite or rutile, thus creating the variations in mineral assemblages and textures
533 observed in some of our samples. The retrograde cooling path may have passed at somewhat
534 lower pressures than estimated in the prior study. Late reaction textures involving fine-grained
535 rutile have developed at relatively low pressures in the antigorite stability field, where rutile
536 also became partly metastable with regard to cafetite/kassite at least in some local
537 environments at the latest recorded stage.
538 The petrogenetic grids presented in this study allow a re-evaluation of the findings in other
539 contact- or regional metamorphic field studies involving Ti- and Zr-minerals. In particular
540 they allow a differentiation between the effects of an earlier regional metamorphism and a
541 subsequent contact metamorphism, and an understanding of how bulk composition
542 differences influenced the formation of “isograds” at the Ballachulish contact aureole,
543 Scotland (Ferry, 1996).
544

ZIRCON AND TITANITE IN OLIVINE-BEARING MARBLES

To our knowledge, coexistence of zircon with olivine in regional metamorphic marbles has been reported only once in the literature (Copjakova et al. 2008). Smooth, uncorroded grain boundaries between olivine and its zircon inclusions in sample 4RA28 are a strong indication for stable coexistence of the two phases in equilibrium, which is in keeping with evidence from (meta-) peridotites, the zircon content of which is regularly used for age dating of both igneous and metamorphic overprint stages and with some experimental evidence (Ferry et al., 2002). The grid presented here fully confirms that zircon can be stable under quartz-undersaturated conditions. Even though reactions like zircon + dolomite = baddeleyite + forsterite + calcite + CO_2 (Ferry 1996) have not yet been determined directly in experiment, the existing field and experimental evidence demonstrates that the stability field of zircon is considerably reduced in quartz-undersaturated rocks and baddelyite and other more complex Zr-bearing minerals like zirconolite become stable at metamorphic temperatures whereas the equilibrium curve for zircon = baddeleyite + SiO_2 lies way beyond 1000°C.

Coexistence of titanite with forsteritic olivine is apparently rare and was so far only reported from exotic magmatic rocks (highly alkaline intrusives, lamprophyres, kimberlites, carbonatites), where titanite is usually not the only Ti-mineral but occurs together with ilmenite, perovskite, titanomagnetite, ulvöspinel or Ti-andradite (Deer et al., 1982; Mariano, 1989). In rare instances, olivine and titanite have also been reported from more basic lavas (Benhallou et al. 2008) and gabbro (Dimitrova et al. 2008; Cabella et al. 1997, Xirouchakis et al. 2001). Titanite-olivine assemblages to our knowledge have not yet been reported from marbles or metamorphic rocks in general. In our samples titanite is either the first preserved Ti-mineral (sample 5K3a) or forms directly from rutile and geikielite and is replaced either by a Ti-bearing mineral of the humite group or by various fine-grained late-stage minerals including geikielite-3, rutile, kassite and serpentine. The coarse grain size of titanite and replacement by humite-group minerals indicates stability at relatively high P-T conditions, i.e

coexisting with olivine before the onset of serpentinization. The petrogenetic grids constructed during this study demonstrate that both titanite and zircon have large stability ranges in olivine-bearing marbles. They should be much more common and will most likely be found more frequently if carefully looked for. Their usefulness for geothermobarometry and geochronology should make such a search rewarding.

IMPLICATIONS

Ti- and Zr-bearing accessory minerals record in their reaction textures part of the metamorphic history of a rock and should be included in any geothermobarometric evaluation to obtain refined information about the metamorphic path. Simple petrogenetic grids like the one constructed here for calcite-dolomite marbles with forsterite/antigorite in excess and including those Ti- and Zr-minerals for which thermodynamic data are known (rutile, titanite, geikielite, zircon and baddeleyite) can be used to delineate the general stability fields. Due to the simple chemical formulas of most of these Ti- and Zr-minerals, many of the univariant reactions are fluid-independent and hence highly suitable for geothermobarometry. In Addition, several of these univariants are pressure-sensitive and can provide valuable barometric information that is usually not easy to get from the main mineral assemblage, at least in impure marbles. The lack of thermodynamic data for zirconolite endmembers, and for F- and Ti-bearing minerals of the humite group are limitations and perhaps worthwhile fields of future experimental research. Titanite activity in particular has a dominant influence on many equilibria and a better understanding of its activity-composition relationships in the system Ti-Si-Al-Fe-Ca-F-H-O – even though subject of some studies (Tropper et al. 2002, Troitzsch and Ellis 2002) – is still highly desirable.

ACKNOWLEDGEMENTS

The first author wants to gratefully acknowledge the financial support for this work by Austrian Science Fund project P22479-N21. Kurt Krenn is thanked for collecting the Raman spectra.

REFERENCES

Armstrong, J.T. (1995) CITZAF: a package of correction programs for the quantitative electron microbeam X-ray analysis of thick polished materials, thin films, and particles: Microbeam Analysis, 4, 177-200.

Bauer, C., Rubatto, D., Krenn, K., Proyer, A., and Hoinkes, G. (2007) A zircon study from the Rhodope metamorphic complex, N-Greece: Time record of a multistage evolution. Lithos, 99, 207-228.

Baziotis, I., Mposkos, E., and Asimow, P.D. (2008) Petrogenesis of ultramafic rocks from the ultrahigh-pressure metamorphic Kimi Complex in Eastern Rhodope (NE Greece). Journal of Petrology, 49, 885-909.

Benhallou, A.Z., Azzouni-Sekkal, A., Liegeois, J.-P., and Bonin, B. (2008) Mineralogy of the Cenozoic Manzaz volcanic province (Latea metacraton, Hoggar, Algeria) International Geological Congress 2008, abstract 1344992.

Cabella, R., Gazzotti, M., and Lucchetti, G. (1997) Loveringite and baddeleyite in layers of chromian spinel from the Bracco ophiolitic unit, Northern Appenines, Italy. The Canadian Mineralogist, 35, 899-908.

Connolly J.A.D. (1990) Multivariable phase diagrams: an algorithm based on generalized thermodynamics. American Journal of Science, 290, 666-718.

Connolly J.A.D. (2005) Composition of phase equilibria by linear programming: tool for geodynamic modelling and its application to subduction zone decarbonation. Earth and Planetary Science Letters, 236, 524-541.

Copjakova, R., Vrana, S., Houzar, S., Cerveny, A., and Malec, J. (2008) Zirconolite, Baddeleyite and geikielite in clinohumite-spinel-forsterite marbles near Horazdivice and

622 Prachatice in southwestern Bohemia. Acta Musei Moraviae, Scientiae Geologicae, 83, 37-
623 51.
624 Deer, W.A., Howie, R.A., and Zussman, J. (1982) Rock-forming minerals, Vol. 1A,
625 Orthosilicates, 2nd edition. Longman, London.
626 Dimitrova, D., Mladenova, V, Hecht, L., Kerestedjian, T., and Machev, P. (2008) Accessory
627 Fe-Ti oxides in the Pilatovets Gabbro from the island-arc volcano-sedimetary sequence
628 unconformably overlaying the Balkan-Carpathian Ophiolite. International Geological
629 Congress 2008, abstract 1208483.
630 Dunn, S.R. (2005) Calcite-graphite isotope thermometry in amphibolites-facies marble.
631 Journal of metamorphic Geology, 23, 813-827.
632 Ehlers, K., and Hoinkes, G. (1987) Titanian chondrodite and clinohumite in marbles from the
633 Ötztal Crystalline Basement. Mineralogy and Petrology, 36, 13-25.
634 Evans, H.T.Jr., Dwornik, E.J., and Milton, C. (1986) Kassite from the Diamond Jo quarry,
635 Magnet Cove, Hot Springs County, Arkansas: The problem of cafetite and cassite.
636 Ferry, J.M. (1996) Three novel isograds in metamorphosed siliceous dolomites from the
637 Ballachulish aureole, Scotland. American Mineralogist, 81, 485-494.
638 Ferry, J.M., Newton, R.C., and Manning, C.E. (2002) Experimental determination of the
639 equilibria: rutile + magnesite + geikielite + CO_2 and zircon + 2 magnesite = baddeleyite +
640 forsterite + 2 CO_2. American Mineralogist, 87, 1342-1350.
641 Franz, G., and Ackermand, D. (1980) Phase relations and metamorphic history of a
642 clinohumite-chlorite-serpentinite-marble from the Western Tauern Area,(Austria).
643 Contributions to Mineralogy and Petrology, 75, 97-110.
644 Fraser, G.L., Pattison, D.R.M., and Heaman, L.M. (2004) Age of the Ballachulish and
645 Glencoe Igneous Complexes (Scottish Highlands), and paragenesis of zircon, monazite and
646 baddeleyite in the Ballachulish aureole. Journal of the Geological Society of London, 161,
647 447-462

Garnier, V. Maluski, H., Giuliani, G., Ohnenstetter, D., and Schwarz, D. (2006) Ar-Ar and U-Pb ages of marble-hosted ruby deposits from central and southeast Asia. Canadian Journal of Earth Sciences, 43, 509-532.

Gieré, R. (1986) Zirconolite, allanite and hoegbomite in a marble skarn from the Bergell contact aureole: implications for mobility of Ti, Zr and REE. Contributions to Mineralogy and Petrology, 93, 459-470.

Gieré, R. (1989) Hydrothermal mobility of Ti, Zr and REE: examples from the Bergell and Adamello contact aureoles (Italy). Terra Nova, 2, 60-67

Gieré, R., Williams, C.T., and Lumpkin, G.R. (1998) Chemical characteristics of natural zirconolite. Schweizerische Mineralogische und Petrographische Mitteilungen, 78, 433-459.

Grey, I.E., Mumme W.G., Pekov I.V., and Pushcharovsky D.Yu. (2003) The crystal structure of chromian kassite from the Saranovskoye deposit, Northern Urals, Russia. American Mineralogist, 88, 1331-1335.

Holland, T. J. B., and Powell, R. (1998) An internally consistent thermodynamic data set for phases of petrological interest. Journal of Metamorphic Geology, 16, 309–343.

Liu. F.L., Gerdes, A., Liou, J.G., Xue, H.M., and Liang, F.H. (2006) SHRIMP U-Pb zircon dating from Sulu-Dabie dolomitic marble, eastern China: constraints on prograde, ultrahigh-pressure and retrograde metamorphic ages. Journal of metamorphic Geology, 24, 569-589.

Katayama, I., Ohta, M., and Ogasawara, Y. (2002) Mineral inclusions in zircon from diamond-bearing marble in the Kokchetav massif, northern Kazakhstan. European Journal of Mineralogy, 14, 1103-1108.

Kato, A., and Matsubara, S. (1991) Geikielite, baddeleyite and zirconolite in dolomitic marble from the Neichi mine, Miyako City, Iwate Prefecture, Japan. Bulletin of the National Science Museum, Tokyo, Series C, 17, 11-20

Krenn, K., Bauer, C., Proyer, A., Klötzli, U., and Hoinkes, G. (2010) Tectonometamorphic evolution of the Rhodope orogen. Tectonics, 29, TC4001, doi:10.1029/2009TC002513

Krivovichev S.V., Yakovenchuk V.N., Burns P.C. Pakhomovsky Y.A., and Menshikov Y.P. (2003) Cafetite, $Ca[Ti_2O_5](H_2O)$: Crystal structure revision of chemical formula. American Mineralogist, 88, 424-429.

Mariano, A.N. (1989) Nature of economic mineralization in carbonatites and related rocks. In: Carbonatites, (Ed. Bell, K.), Unwin Hyman, London.

Mitchell, R.H., and Chakhmouradian, A.R. (1998) Instability of perovskite in a CO_2-rich environment ; examples from carbonatite and kimberlite. The Canadian Mineralogist, 36, 939-951.

Mposkos, E., and Kostopoulos, D. (2001) Diamond, former coesite and supersilicic garnet in metasedimentary rocks from the Greek Rhodope: a new ultrahighpressure metamorphic province established. Earth and Planetary Science Letters, 192, 497–506.

Mposkos, E., and Krohe, A. (2006) Pressure-temperature-time paths of closely associated ultra-high-pressure diamond-bearing crustal and mantle rocks of the Kimi Complex: implications for the tectonic history of the Rhodope Mountains, northern Greece. Canadian Journal of Earth Sciences, 43, 1755–1776.

Mposkos, E., Baziotis, I., Proyer, A., and Hoinkes, G. (2006) Dolomitic marbles from the ultrahigh-presure metamorphic Kimi Complex, N.E. Greece. Mineralogy and Petrology, 88, 341–362.

Nishio, D., and Minakawa, T. (2004) Baddeleyite, zirconolite and calcirtite in lateritic rocks from Ryoke and Chichibu Terranes, Japan. Journal of Mineralogical and Petrological Sciences, 99, 42-53.

Pascal, M-L., Di Muro, A., Fonteilles, M., and Principe, C. (2009) Zirconolite and calcirtite in banded forsterite-spinel-calcite skarn ejecta from the 1631 eruption of Vesuvius: inferences for magma-wallrock interactions. Mineralogical Magazine, 73, 333-356.

Perraki, M., Proyer,A. ,Mposkos, E.,Kaindl, R., and Hoinkes, G. (2006) Raman microspectroscopy on diamond, graphite and other carbon polymorphs from the ultrahigh-pressure metamorphic Kimi-Complex of the Rhodope Metamorphic Province, NE Greece. Earth and Planetary Science Letters, 241, 672–685.

Popova, V.I., Popov, V.A., and Kanonerov A.A. (1998) Chromium-bearing kassite from the Saranovskoye deposit – a first finding from the Urals. Miass, 2, 75-77.

Powell, R., and Holland, T.J.B. (1994) Optimal geothermobarometry. American Mineralogist, 79, 120-133.

Powell, R., Holland, T., andWorley, B. (1998) Calculating phase diagrams involving solid solutions via non-linear equations, with examples using THERMOCALC. Journal of Metamorphic Geology 16, 577–588.

Proyer, A., Mposkos, E., Baziotis, I., and Hoinkes, G. (2008) Tracing high-pressure metamorphism in marbles: Phase relations in high-grade aluminous calcite–dolomite marbles from the Greek Rhodope massif in the system $CaO–MgO–Al_2O_3–SiO_2–CO_2$ and indications of prior aragonite. Lithos, 104, 119-130.

Purtscheller, F., and Tessadri, R. (1985) Zirconolite and baddeleyite from metacarbonates of the Oetztal-Stubai complex (northern Tyrol, Austria). Mineralogical Magazine, 49, 523-529.

Ribbe, P. (1982) The humite series and Mn-analogues. In: Reviews in Mineralogy Vol 5 (2^{nd} edition) Orthosilicates. Ed. P.H. Ribbe, Mineralogical Society of America.

Troitzsch, U., and Ellis, D.J. (2002) Thermodynamic properties and stability of AlF-bearing titanite CaTiOSiO4-CaAlFSiO4. Contributions to Mineralogy and Petrology, 142, 543-563.

Tropper, P., Harlov, D., Krenn, E., Finger, F., Rhede, D., and Bernhard, F. (2007) Zr-bearing minerals as indicators of the polymetamorphic evolution of the eastern, lower Austroalpine

nappes (Stubenberg Granit contact aureole, Styria, Eastern Alps, Austria). Lithos, 95, 72-86.

Tropper, P., Manning, C.E., and Essene, E.J. (2002) The substitution of Al and F in titanite at high pressure and temperature: experimental constraints on phase relations and solid solution properties. Journal of Petrology 43, 1787-1814.

Sastna, A., and Prikryl, R. (2009). Decorative marbles from the Krkonose-Jizera terrane (Bohemian Massif, Czech Republic): provenance criteria. International Journal of Earth Sciences, 98, 357-366.

Stucki, A., Trommsdorff, V., and Günther, C. (2001) Zirconolite in metarodingites of Penninic Mesozoic ophiolites, Central Alps. Schweizerische Mineralogische und Petrographische Mitteilungen, 81, 257-265.

Whitney, D.A., and Evans, B.W. (2010) Abbreviations for names of rock-forming minerals. American Mineralogist 95, 185-187.

Williams, C.T., and Gieré, R. (1988) Metasomatic zonation of REE in zirconolite from a marble skarn at the Bergell contact aureole (Switzerland/Italy). Schweizerische Mineralogische und Petrographische Mitteilungen, 68,133-140.

Young, E.D., and Morrison, J. (1992) Relations among net-transfer reaction progress ^{18}O – ^{13}C depletion, and fluid infiltration in a clinohumite-bearing marble. Contributions to Mineralogy and Petrology, 111, 391-408.

Xirouchakis, D., Lidsley, D.H., and Frost, B.R. (2001) Assemblages with titanite ($CATiSiO_5$), Ca-Mg-Fe olivine and pyroxenes, Fe-Mg-Ti oxides, and quartz: Part II. Application. American Mineralogist, 86, 254-264.

Zhang, A.C., Taylor, L.A., Wang, R.C., Li, Q.L., Li, X.H., Patchen, A.D., and Liu, Y. (2012) Sims Pb/Pb ages of baddeleyite and zirconolite in Apollo 17 norite 78235: implications for shock histories of extraterrestrial rocks. 43rd Lunar and Planetary Sciences Conference, Abstract # 1036.

751

752

753 **Figure captions:**

754

755 Figure 1: geotectonic map of the Greek part of the Rhodope mountains: Diamond-bearing
756 gneisses of the Kimi-UHP-unit indicated by black diamond symbols; the calcite-
757 dolomite marble location near Organi village is indicated by the flower-symbol.

758

759 Figure 2 (sample 4RA28): a) olivine-chlorite intergrowth with diopside rim and younger
760 amphibole; b) zircon inclusion in olivine; c) slightly zoned matrix zircon with thorianite
761 and carbonate inclusions; d) thorianite inclusions in the BSE-brighter zone of zircon; e)
762 complex zoning pattern of zircon in Figure 2b. Mineral abbreviations are according to
763 Whitney & Evans (2010).

764

765 Figure3 (sample 5K3): a) olivine overgrown by Ti-clinohumite and partly serpentinized; b)
766 diopside with inclusions of Mg-free calcite, contained in dolomite; c) matrix titanite,
767 slightly retrogressed to rutile + calcite + serpentine; d) titanite replaced by Ti-
768 clinohumite; e) late stage pseudomorphs of rutile + serpentine + geikielite after titanite;
769 f) pseudomorphs of serpentine + rutile + dolomite after Ti-clinohumite; g-j: zirconolite
770 in various forms of intergrowth with zircon, euxenite, titanite and thorianite; k)
771 zirconolite single crystal (inclusion in a large chlorite) with BSE-zoning mainly due to
772 variable Th-content (colour inset: red = high Th, yellow = lower Th). Numbers
773 correspond to points of analyses given in Table 2.

774

775 Figure 4 (sample 5K6a1: a) rutile inclusion in spinel; b) rutile partly exposed to the matrix
776 and transformed to geikielite + zirconolite; c) rutile near spinel, transformed into three

777 textural types of geikielite/ilmenite; d) large rutile grain transformed into geikielite-1
778 and complex polymineralic pseudomorphs; e-g) rutile with three types of geikielite-
779 ilmenite and relics of titanite; h) complex double-pseudomorph of type-3 geikielite-
780 ilmenite; i) detail of 4d showing variability of type-3 geikielite-ilmenite compositions
781 by BSE contrast; j) detail of 4d showing 3 types of pseudomorphing reactions (see text);
782 k) geikielite-1 with geikielite-3 rim; l) rutile-geikielite-1 intergrowth with geikielite-2
783 developing towards chlorite matrix and geikielite-ilmenite-3 towards serpentine (former
784 olivine); m) detail of 4l shows titanite in geikielite-2 textural setting.
785
786 Figure 5 (sample 5K6a2): Diopside rim around partly serpentinized olivine, with some
787 additional amphibole; b) large amphibole with some diopside inclusions and hundreds
788 of small BSE-bright rutile inclusions, perhaps after former Ti-clinohumite; c) rutile
789 overgrown by titanite which partly retrogresses to geikielite-3 or rutile-2 (minute BSE-
790 bright streaks and dots) at the margins; d) like (c), but titanite with zirconolite-inclusion
791 and decomposition to kassite; e) rutile+geikielite-1 overgrown by titanite, partly
792 decomposing to ilmenite + calcite + serpentine; f) titanite partly replaced by laths of
793 kassite + calcite + serpentine.
794
795 Figure 6 (sample 5K6b): a) rutile overgrown by titanite + zirconolite; b) rutile (unaltered) and
796 titanite partly transformed to ilmenite-3 in serpentine; c) rutile-geikielite-1 intergrowth
797 next to a partial and a complete pseudomorphs after titanite; d) detail of (6c): type-2
798 intergrowth of rutile and/or titanite with chlorite, with rutile replacing titanite (left side
799 and in large ellipse).
800

Figure 7: Raman spectrum of kassite/cafetite (black line) and titanite (red line). The remaining characteristic bands (not belonging to titanite, carbonate or serpentine or overlapping with these) are underlined.

Figure 8: a) Zr-Ca-Ti-diagram for zirconolites from samples 5K3 (dots) and 5K6a1 (crosses) and b) detail of the diagram; c) clear positive correlation of actinides (Th + U) with total Fe and d) with Mg + Mn.

Figure 9: a) triangular plot of actinides versus rare earth elements and (Nb^{5+} + Ta^{5+}); b) best correlation found for rare earths is with total Fe; c) best correlation found for (Nb^{5+} + Ta^{5+}) is also with total Fe; d) best correlation found for Al is with Ti: positive for 5K3 and negative for 5K6a1.

Figure 10: Partial petrogentic grid in the system TiO_2-CaO-MgO-Al_2O_3-SiO_2-CO_2-H_2O (TCMASCH) for calcite-dolomite marbles with olivine- or serpentine-predominance (SiO_2-undersaturated), showing the stability fields of geikielite, rutile and titanite. Mineral abbreviations are according to Whitney & Evans (2010). Invariant points named consecutively as IP1 to IP7. IP3 and IP5 are in the CMSCH subsystem.

Fig 11: Invariant point 1 (IP1 from Fig. 10) with all possible univariants around it. Points on the univariants show the shift of IP1 with the deviation of one of the endmembers from unit activity, illustrating the sensitivity of reaction curves to mineral compositions. Mineral abbreviations like in Fig. 10; the numbers indicate activity values.

Figure 12: Partial petrogentic grid in the system ZrO_2-CaO-MgO-Al_2O_3-SiO_2-CO_2-H_2O (ZCMASCH) for calcite-dolomite marbles with olivine- or serpentine-predominance (SiO_2-undersaturated), showing the stability fields of baddeleyite and zircon.

826 Figure 13: Combined petrogenetic grid in TZCMASCH, including *P-T* conditions derived for
827 samples 5K6a-2 (red ellipse) and 5K3a (area between and including green ellipses). The
828 dashed blue line shows the shift of the reaction bdy + di + dol = zrn + fo + cal if
829 measured mineral compositions for clinopyroxene and olivine in sample 4RA28 are
830 used. The long thick arrow represents the P-T path derived by Proyer et al. (2008) for
831 impure marbles from the same field area.
832
833

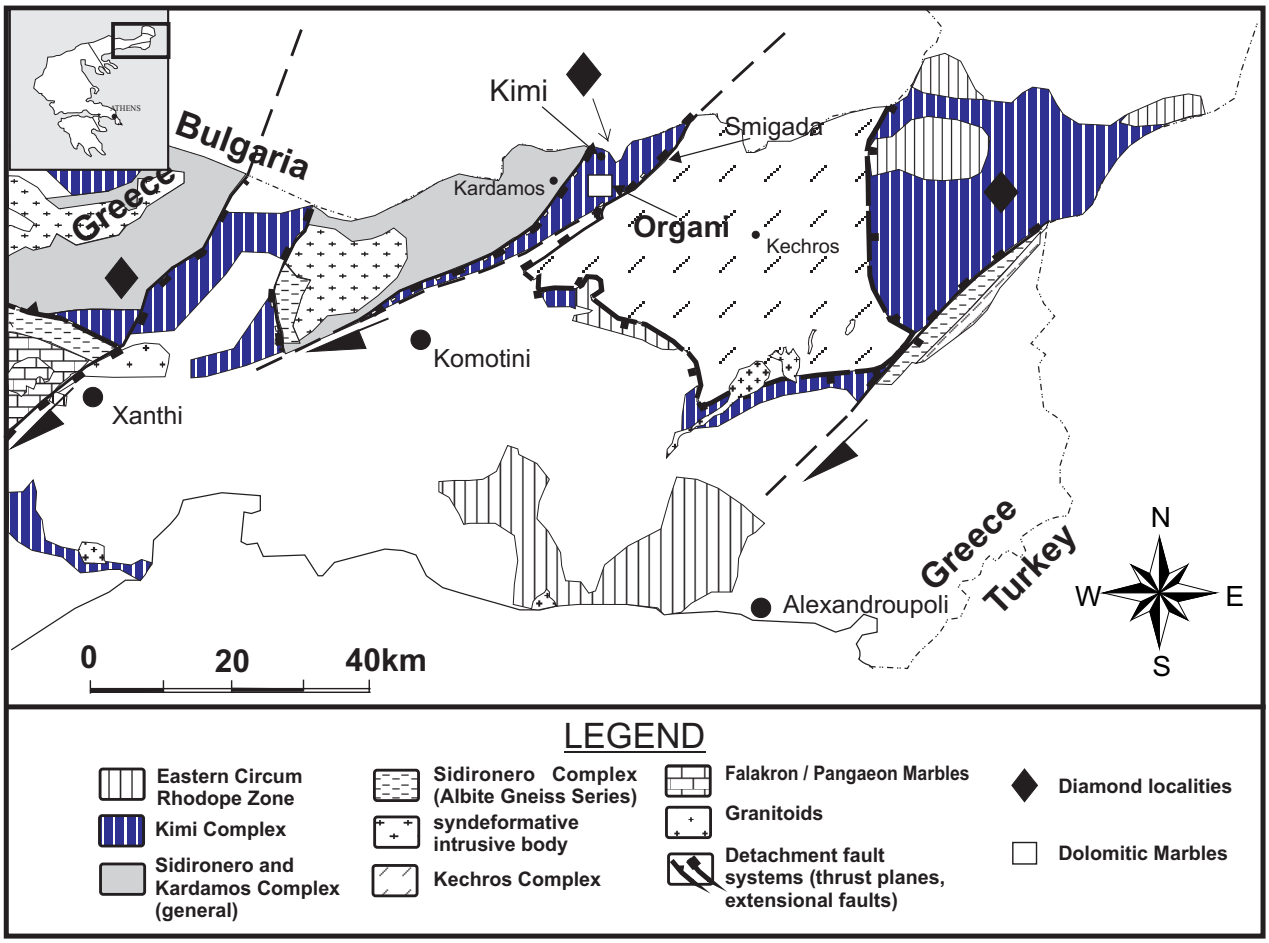
ATHENS
Bulgaria
Greece
Kimi
Smigada
Kardamos
Organi
Kechros
Komotini
Xanthi
Alexandroupoli
Greece
Turkey
N
W
E
S
0
20
40km
LEGEND
Eastern Circum Rhodope Zone
Kimi Complex
Sidironero and Kardamos Complex (general)
Sidironero Complex (Albite Gneiss Series)
syndeformative intrusive body
Kechros Complex
Falakron / Pangaeon Marbles
Granitoids
Detachment fault systems (thrust planes, extensional faults)
Diamond localities
Dolomitic Marbles

Fig.1

Figure 2

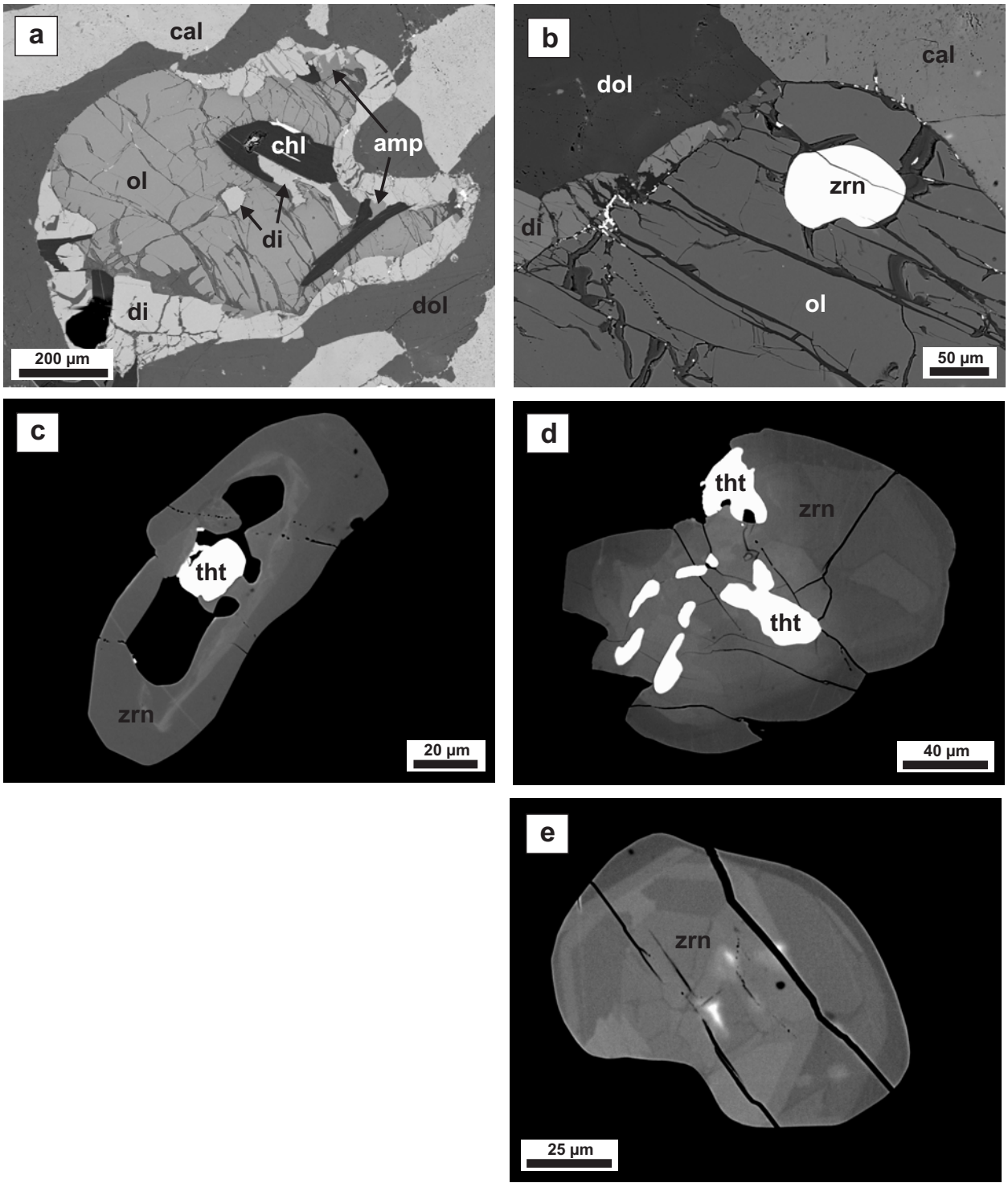
a
cal
chl
amp
ol
di
di
dol
200 µm
b
dol
cal
zrn
di
ol
50 µm
c
tht
zrn
20 µm
d
tht
zrn
tht
40 µm
e
zrn
25 µm

Figure 3a-f

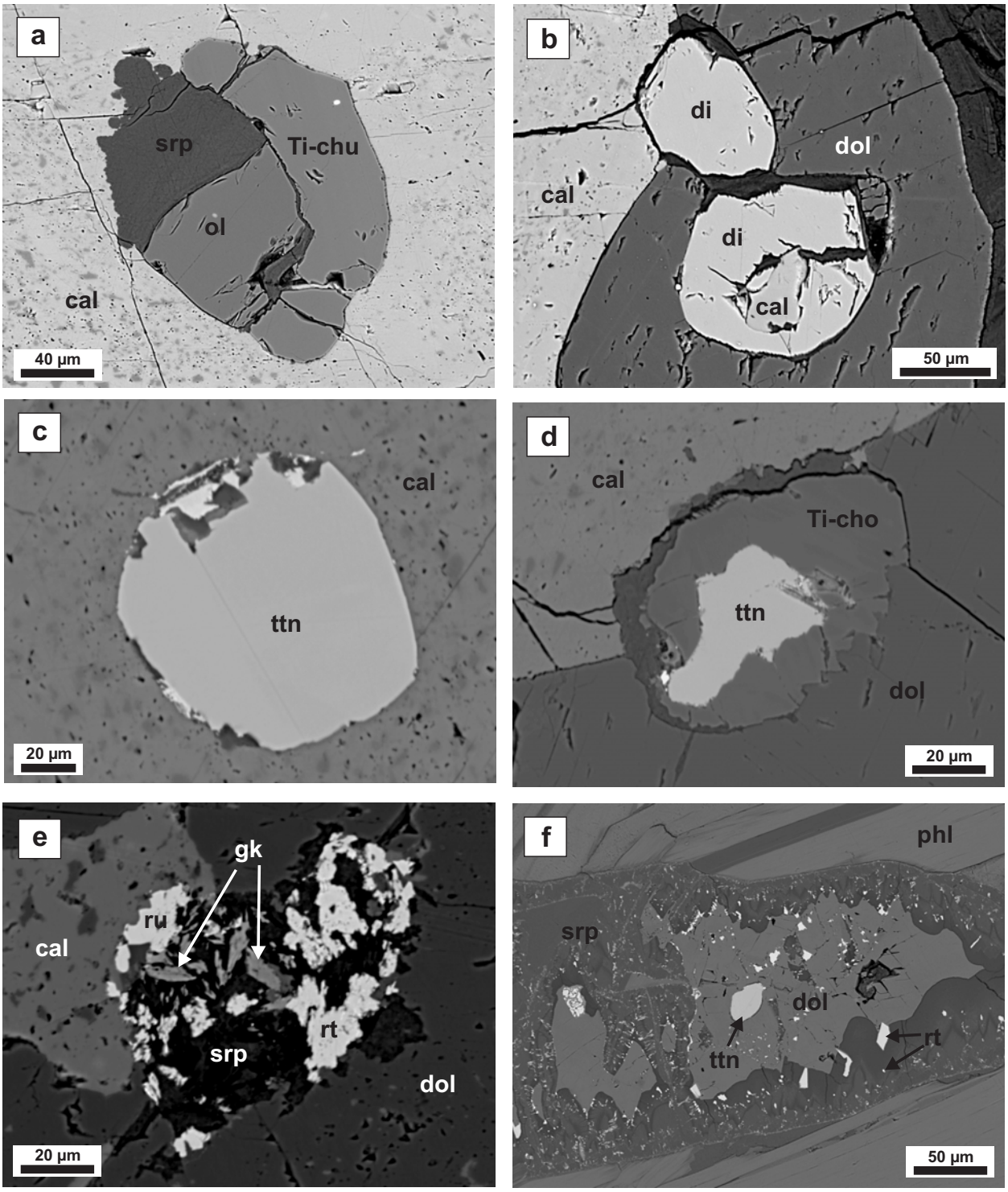
a
srp
Ti-chu
ol
cal
40 µm
b
di
dol
cal
di
cal
50 µm
c
cal
ttn
20 µm
d
cal
Ti-cho
ttn
dol
20 µm
e
gk
ru
cal
rt
srp
dol
20 µm
f
phl
srp
dol
ttn
rt
50 µm

Figure 3g-k

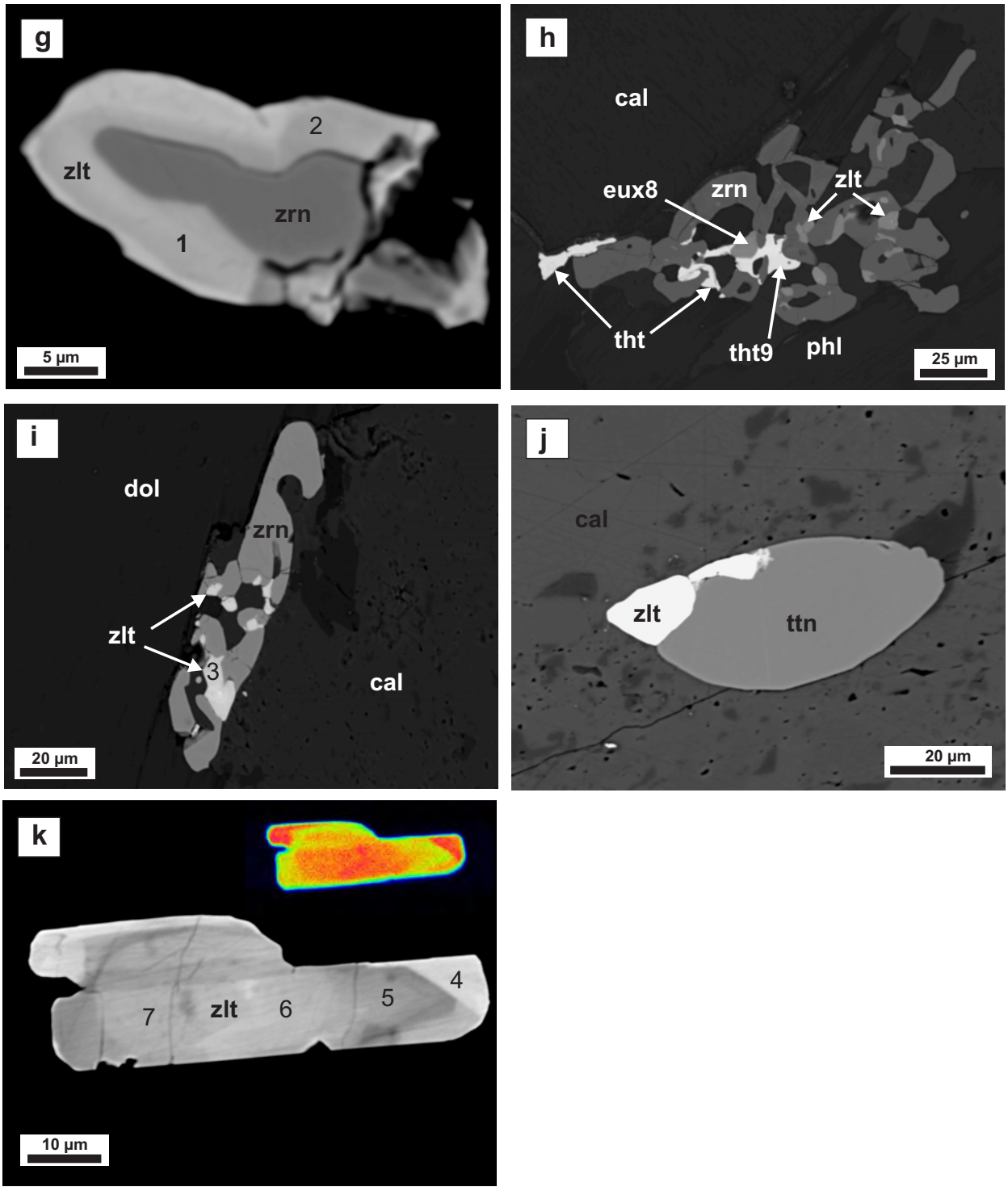
g
2
zlt
zrn
1
5 µm
h
cal
eux8
zrn
zlt
tht
tht9
phl
25 µm
i
dol
zrn
zlt
3
cal
20 µm
j
cal
zlt
ttn
20 µm
k
7
zlt
6
5
4
10 µm

Figure 4

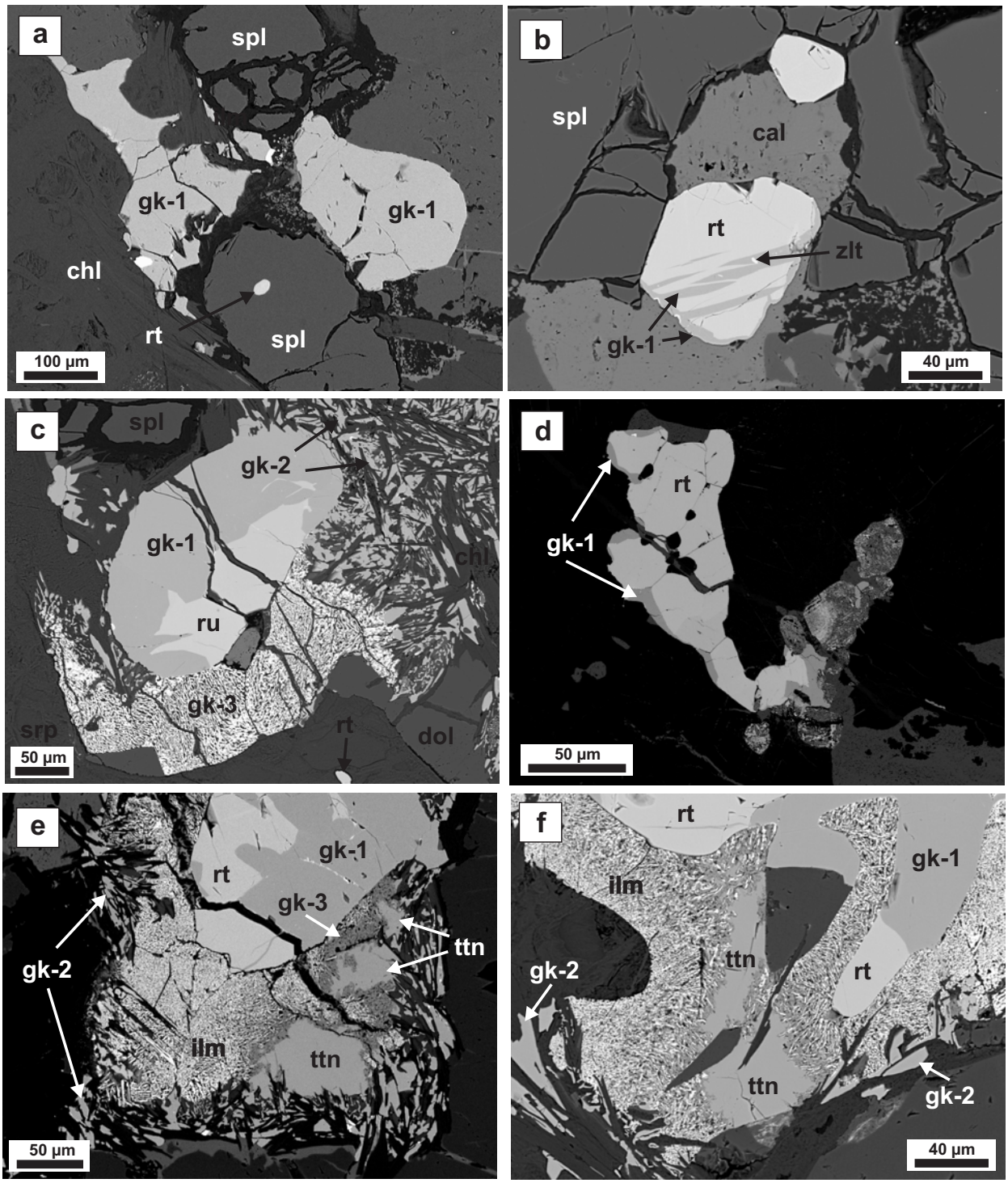
a
spl
gk-1
gk-1
chl
rt
spl
100 µm
b
spl
cal
rt
zlt
gk-1
40 µm
c
spl
gk-2
gk-1
chl
ru
gk-3
srp
rt
dol
50 µm
d
rt
gk-1
50 µm
e
gk-1
rt
gk-3
ttn
gk-2
ilm
ttn
50 µm
f
rt
gk-1
ilm
ttn
gk-2
rt
ttn
gk-2
40 µm

Figure 4 cont

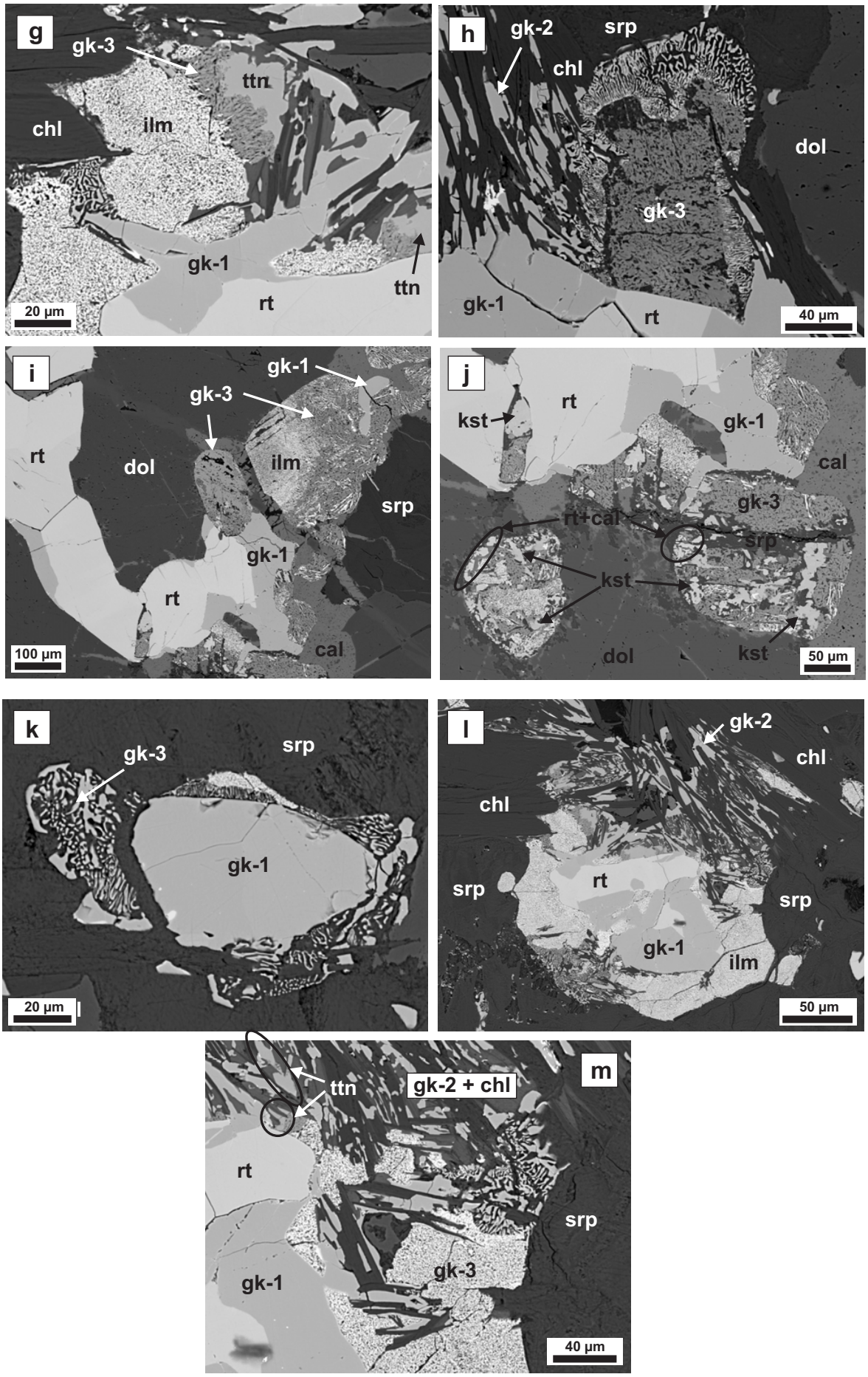

Figure 5

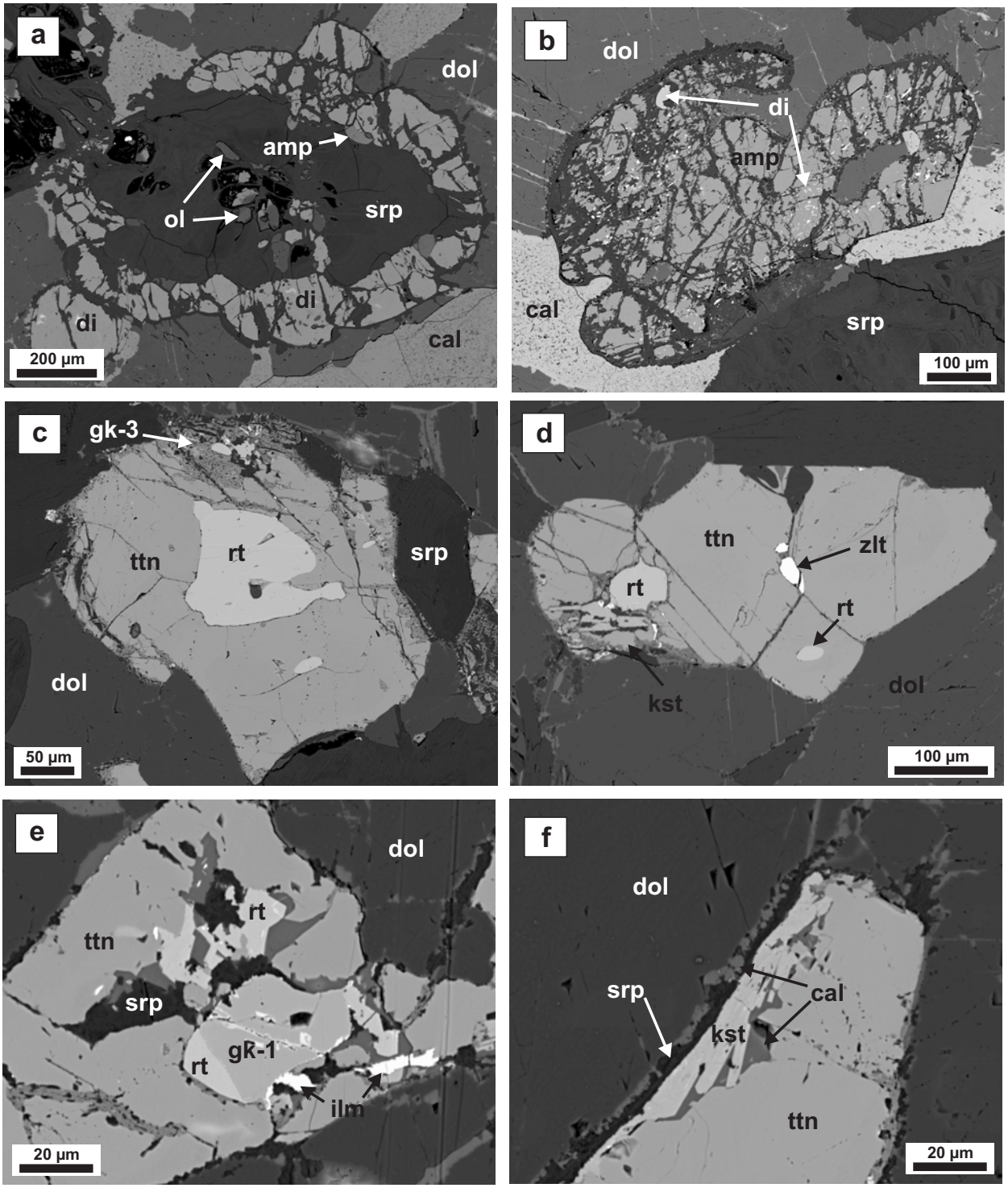
a
dol
amp
ol
srp
di
di
cal
200 µm
b
dol
di
amp
cal
srp
100 µm
c
gk-3
ttn
rt
srp
dol
50 µm
d
ttn
zlt
rt
rt
kst
dol
100 µm
e
dol
rt
ttn
srp
gK-1
rt
ilm
20 µm
f
dol
srp
cal
kst
ttn
20 µm

Figure 6

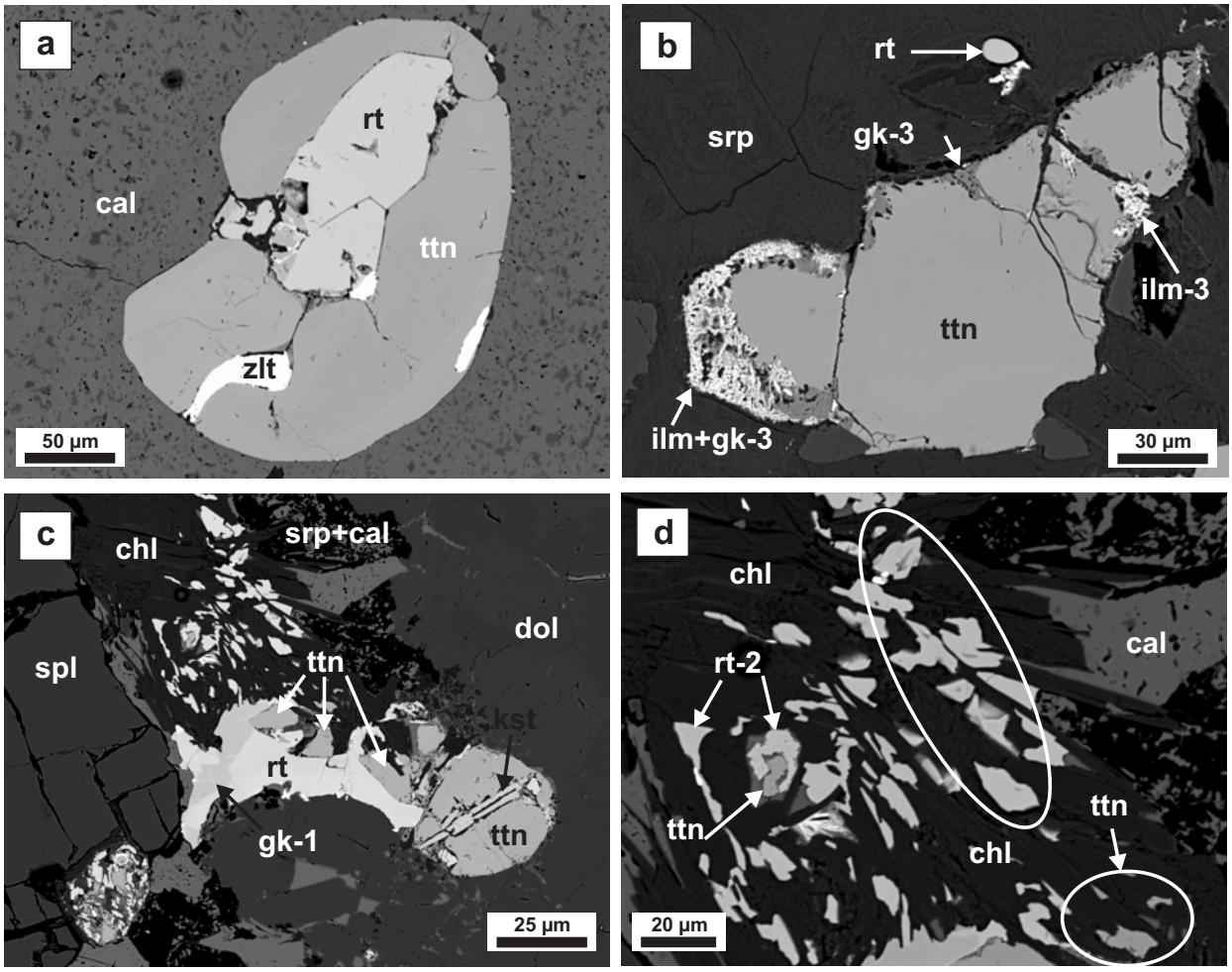
a
rt
cal
ttn
zlt
50 µm
b
rt
srp
gk-3
ilm-3
ttn
ilm+gk-3
30 µm
c
chl
srp+cal
dol
spl
ttn
kst
rt
gk-1
ttn
25 µm
d
chl
cal
rt-2
ttn
chl
ttn
20 µm

Figure 7

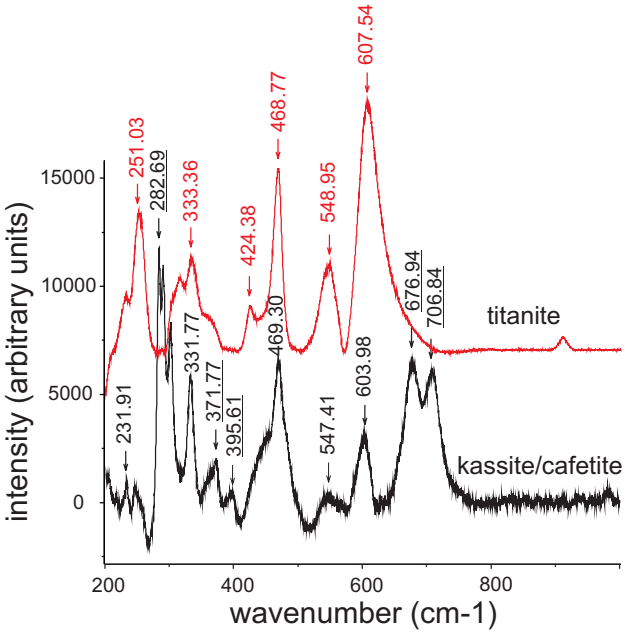
intensity (arbitrary units)
wavenumber (cm-1)
15000
10000
5000
0
200
400
600
800
251.03
282.69
333.36
424.38
468.77
548.95
607.54
676.94
706.84
titanite
231.91
331.77
371.77
395.61
469.30
547.41
603.98
kassite/cafetite

Figure 8a, b

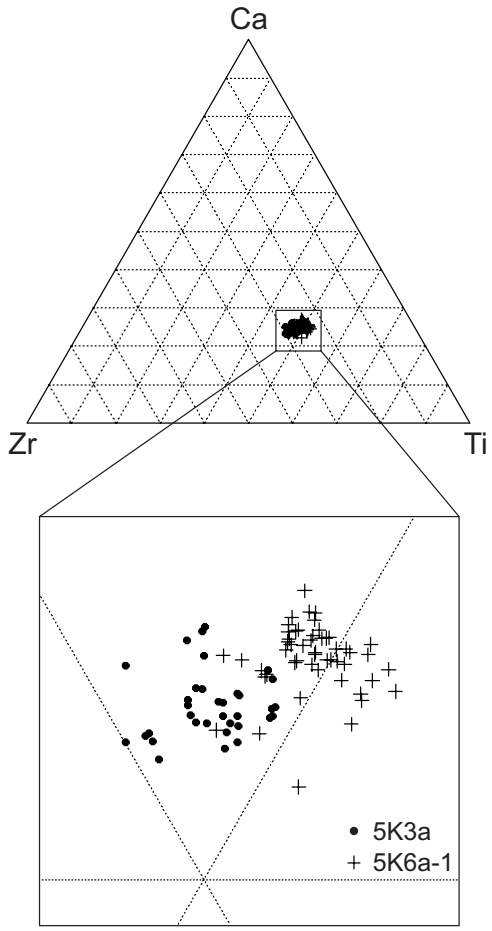

Figure 8c, d

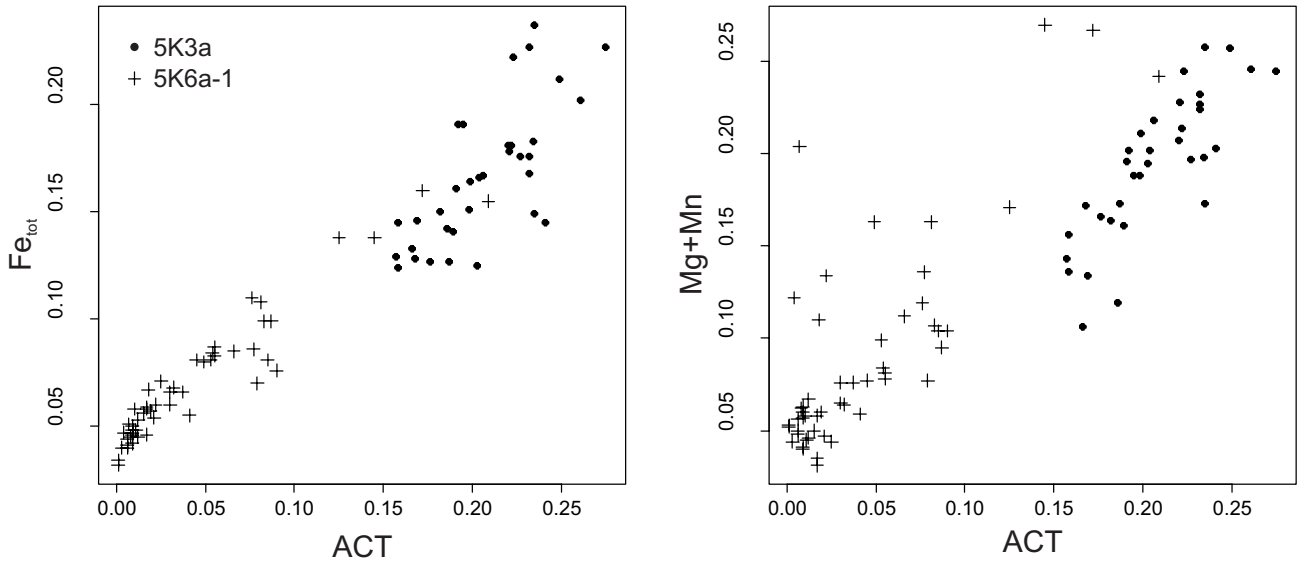

Figure 9a, b

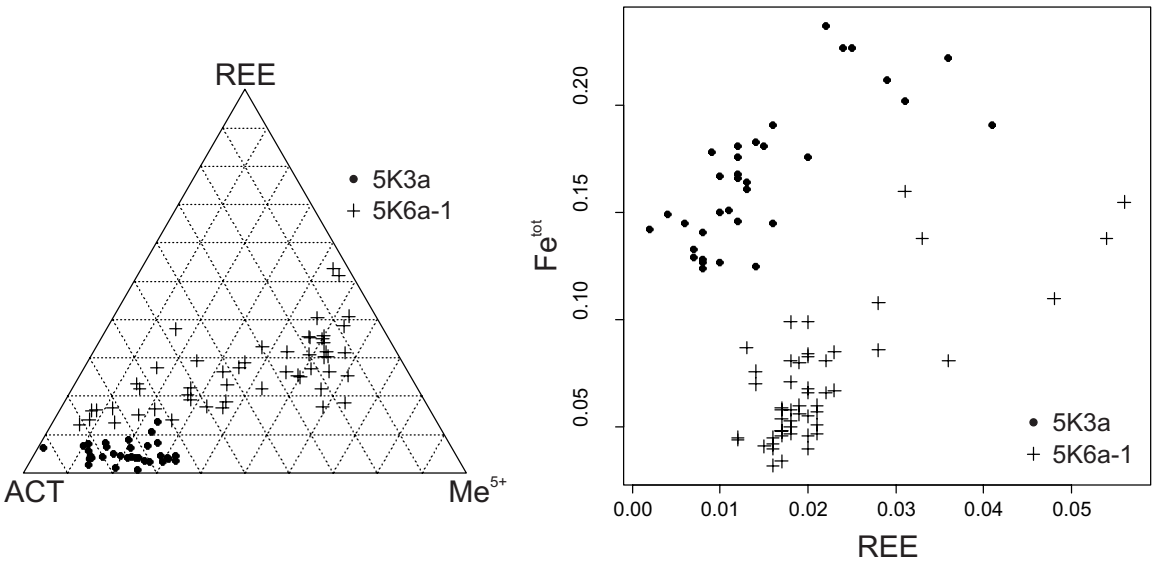

Figure 9c, d

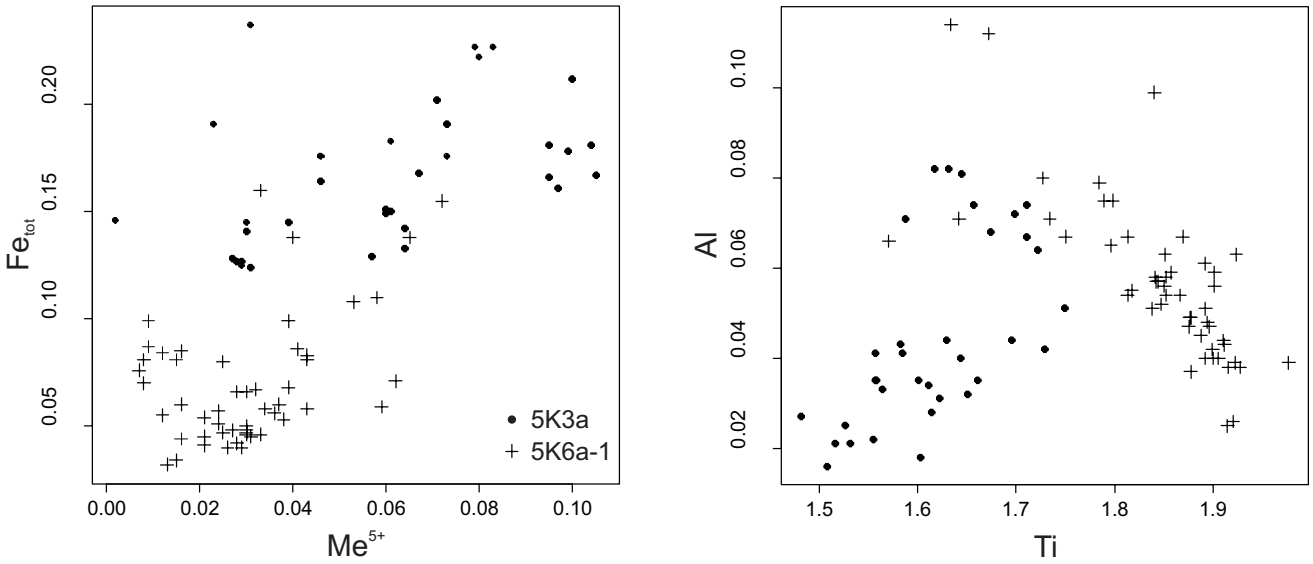

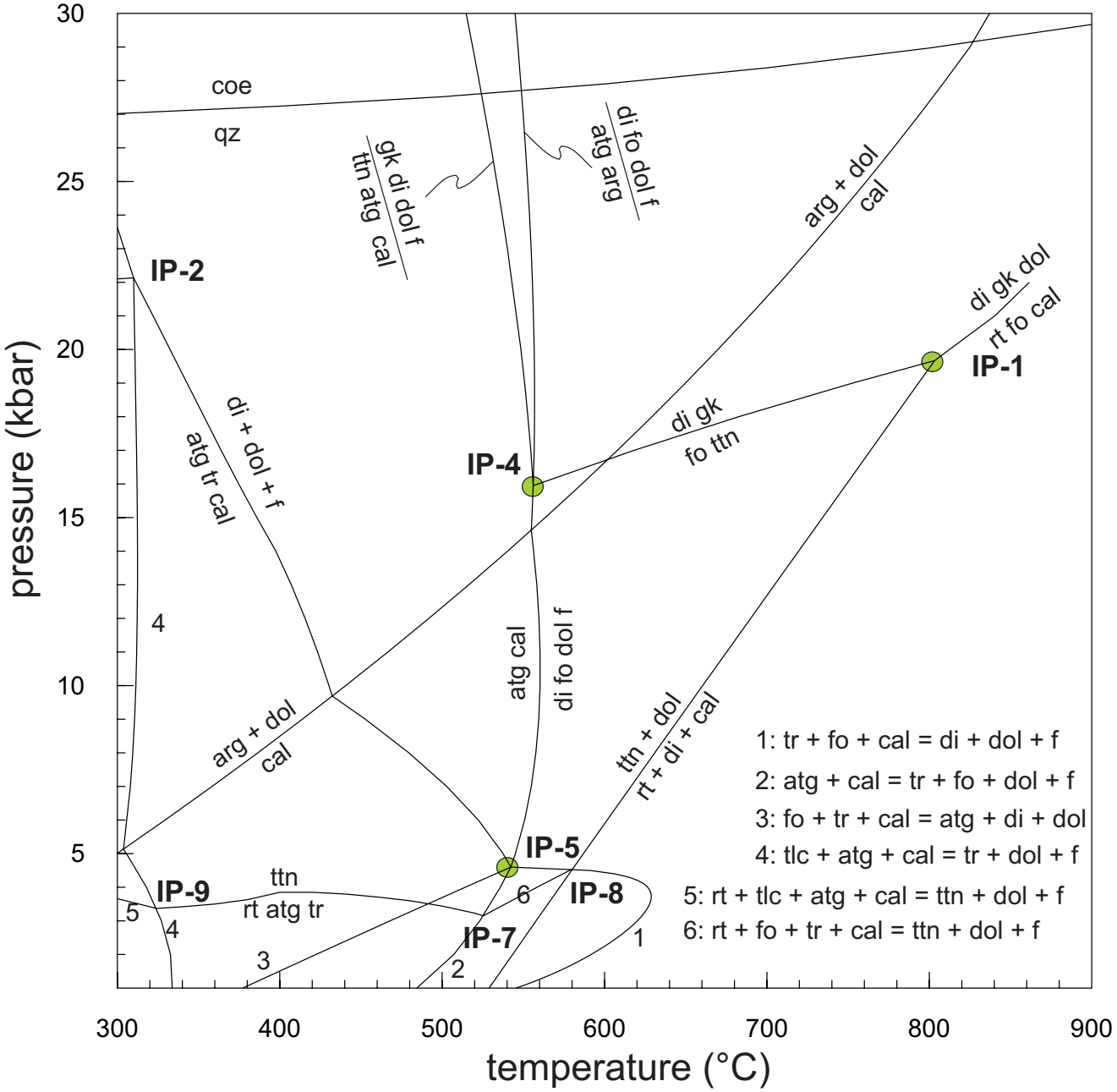
pressure (kbar)
temperature (°C)
30
25
20
15
10
5
300
400
500
600
700
800
900
coe
qz
gk di dol f
ttn atg cal
di fo dol f
atg arg
arg + dol
cal
di gk dol
rt fo cal
IP-1
IP-2
IP-4
di gk
fo ttn
di + dol + f
atg tr cal
atg cal
di fo dol f
arg + dol
cal
ttn + dol
rt + di + cal
IP-5
IP-9
ttn
rt atg tr
IP-8
IP-7
1: tr + fo + cal = di + dol + f
2: atg + cal = tr + fo + dol + f
3: fo + tr + cal = atg + di + dol
4: tlc + atg + cal = tr + dol + f
5: rt + tlc + atg + cal = ttn + dol + f
6: rt + fo + tr + cal = ttn + dol + f

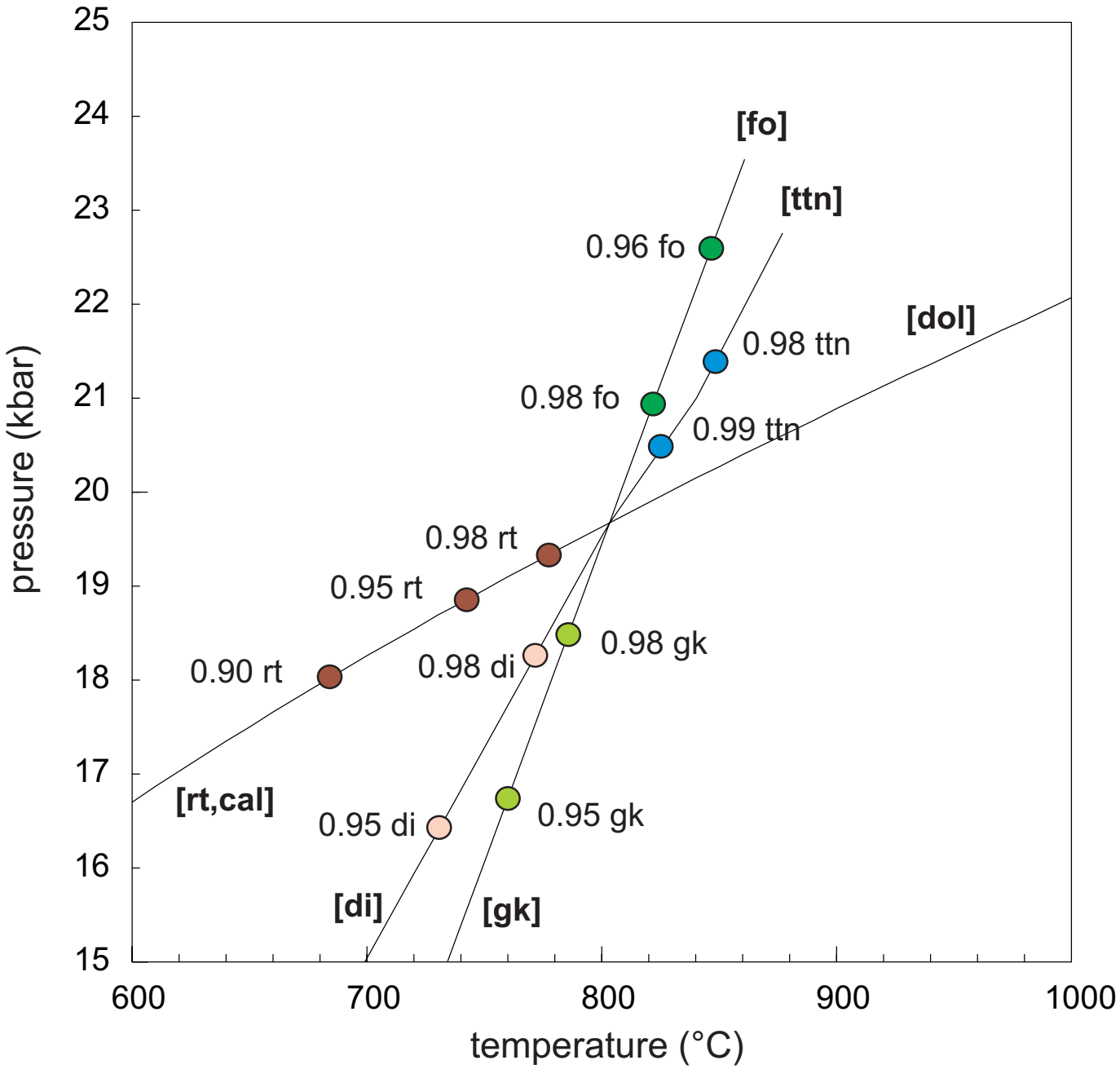
25
24
23
22
21
20
19
18
17
16
15
pressure (kbar)
600
700
800
900
1000
temperature (°C)
[fo]
[ttn]
[dol]
[rt,cal]
[di]
[gk]
0.96 fo
0.98 ttn
0.98 fo
0.99 ttn
0.98 rt
0.95 rt
0.90 rt
0.98 di
0.98 gk
0.95 di
0.95 gk

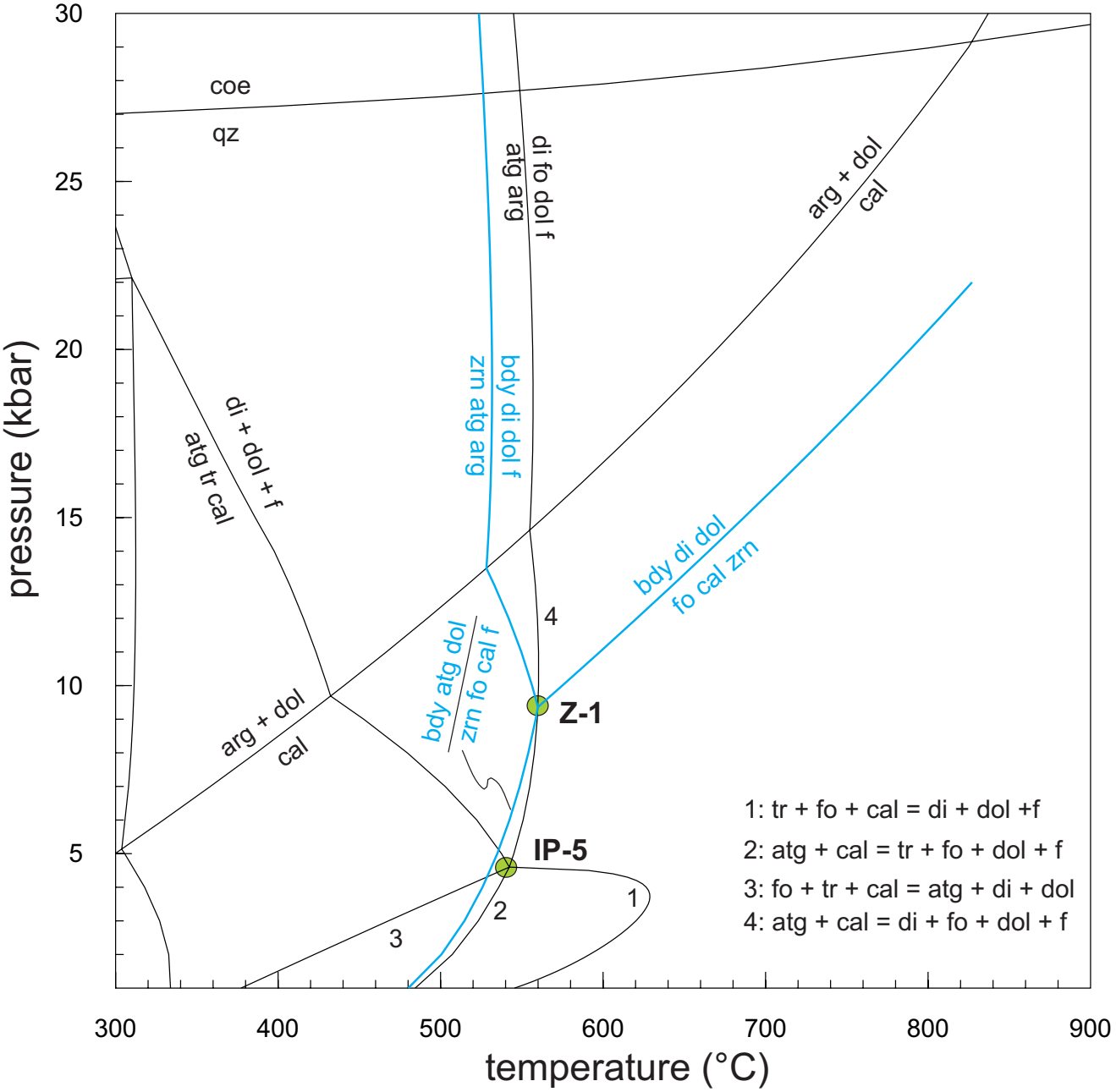
pressure (kbar)
temperature (°C)
30
25
20
15
10
5
300
400
500
600
700
800
900
coe
qz
di fo dol f
atg arg
arg + dol
cal
di + dol + f
atg tr cal
zrn atg arg
bdy di dol f
bdy di dol
fo cal zrn
bdy atg dol
zrn fo cal f
arg + dol
cal
4
Z-1
IP-5
1
2
3
1: tr + fo + cal = di + dol +f
2: atg + cal = tr + fo + dol + f
3: fo + tr + cal = atg + di + dol
4: atg + cal = di + fo + dol + f

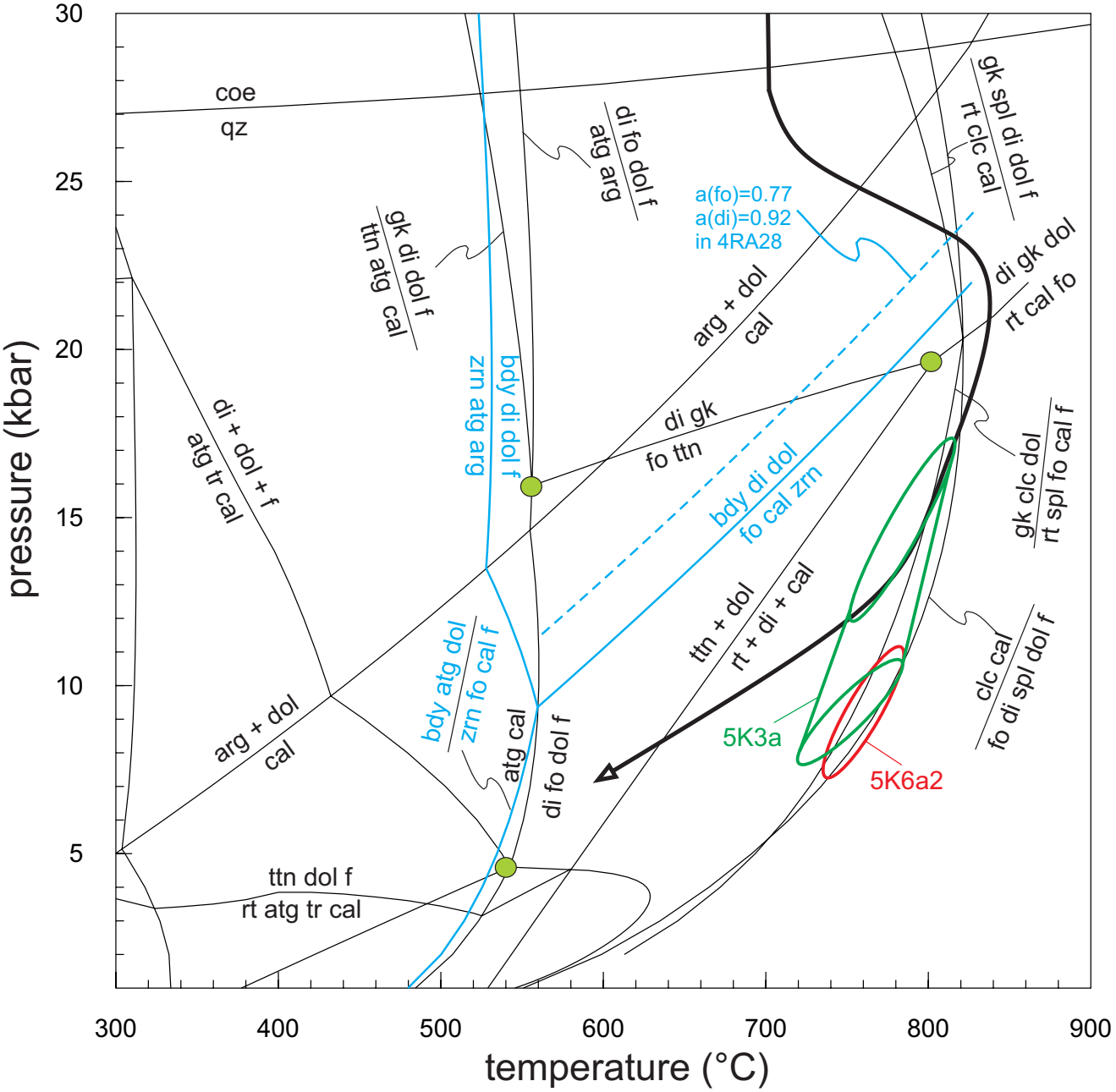
pressure (kbar)
temperature (°C)
30
25
20
15
10
5
300
400
500
600
700
800
900
coe
qz
di fo dol f
atg arg
gk di dol f
ttn atg cal
gk spl di dol f
rt clc cal
a(fo)=0.77
a(di)=0.92
in 4RA28
di gk dol
rt cal fo
arg + dol
cal
di gk
fo ttn
bdy di dol f
zrn atg arg
di + dol + f
atg tr cal
bdy di dol
fo cal zrn
gk clc dol
rt spl fo cal f
ttn + dol
rt + di + cal
bdy atg dol
zrn fo cal f
atg cal
di fo dol f
clc cal
fo di spl dol f
5K3a
5K6a2
arg + dol
cal
ttn dol f
rt atg tr cal

Table 1: Selected SEM (EDS) analyses of geikielite, ilmenite, spinel, chlorite, olivine and diopside

Sample	Fig 4c	Fig 4c	Fig 4c	5K6a1	5K6a2	5K6b	5K6a1	5K6a2	4RA28	4RA28	5K6a2	5K6a2	5K6a2	4RA28
Mineral	gk-1	gk-2l	gk-3	ilm-3	gk-3	spl	chl	ol	ol	chl	cpx	cpx	cpx	cpx
SiO_2	n.d.	n.d.	8.35	0.26	1.04	n.d.	30.70	42.35	40.70	34.36	56.42	55.58	54.41	56.25
TiO_2	64.50	64.16	38.56	54.50	49.00	n.d.	0.39	n.d.	0.05	0.04	n.d.	n.d.	0.36	n.d.
Al_2O_3	n.d.	n.d.	0.74	n.d.	0.41	70.46	20.09	n.d.	n.d.	14.58	0.00	0.89	1.83	0.20
Cr_2O_3	n.d.	n.d.	n.d.	n.d.	n.d.	n.d.	n.d.	n.d.	n.d.	0.05	n.d.	n.d.	n.d.	n.d.
FeO	7.03	8.22	27.05	37.16	9.24	1.81	0.57	1.74	11.75	4.63	0.26	0.20	0.28	1.38
MnO	0.00	0.00	2.72	2.43	n.d.	n.d.	n.d.	n.d.	0.11	n.d.	n.d.	n.d.	n.d.	0.01
MgO	28.48	27.71	9.89	4.21	26.00	27.78	36.21	56.15	47.66	34.91	18.74	18.49	18.19	18.37
CaO	n.d.	n.d.	0.27	0.10	0.36	n.d.	0.12	0.00	0.05	0.02	25.06	25.58	25.25	24.98
Na_2O	n.a.	n.a.	n.a.	n.a.	n.a.	n.a.	n.a.	n.a.	n.a.	n.a.	n.d.	0.05	n.d.	0.00
Total	100.01	100.09	87.58	98.66	86.05	100.04	88.08	100.25	100.31	88.63	100.48	100.79	100.32	101.19
Si	--	--	0.21	0.01	0.02	--	2.83	1.00	1.00	3.20	2.02	1.99	1.96	2.01
Ti	1.00	1.00	0.74	1.01	0.87	--	0.03	--	--	--	--	--	0.01	--
Al	--	--	0.02	--	0.01	1.98	2.18	--	--	1.60	--	0.04	0.08	0.01
Cr	--	--	--	--	--	--	--	--	--	--	--	--	--	--
Fe^{2+}	0.12	0.14	0.51	0.76	--	0.01	0.04	0.03	0.24	0.36	0.01	0.01	0.01	0.04
Fe^{3+}	--	--	0.07	--	0.18	0.02	--	--	--	--	--	--	--	--
Mn	--	--	0.06	0.05	--	--	--	--	--	--	--	--	--	--
Mg	0.88	0.86	0.38	0.15	0.91	0.99	4.97	1.97	1.75	4.84	1.00	0.99	0.97	0.98
Ca	--	--	0.01	--	0.01	--	0.01	--	--	--	0.96	0.98	0.97	0.96
Na	--	--	--	--	--	--	--	--	--	--	--	--	--	--
SumCat	2.00	2.00	2.00	1.99	2.00	3.00	10.06	3.00	3.00	10.00	3.98	4.00	4.00	3.99

n.d. = not detected, n.a. = not analysed; chl = chlorite, cpx = clinopyroxene, gk = geikielite, ilm = ilmenite, ol = olivine, spl = spinel

Table 1 cont.: Selected SEM (EDS) analyses of phlogopite, amphibole, kassite, titanite and humite group minerals

Sample	5K6a1	5K3	5K6a2	5K6a2	5K6b	4RA28	4RA28	5K6a2	5K6a1	Fig 4e	5K6b	Fig 4g	Fig. 3a	Fig. 3d	5K3
Mineral	phl	phl	amp	amp	amp	amp	amp	kst	ttn	ttn	ttn	ttn	Ti-chu	Ti-cho	Ti-hu
SiO_2	39.87	41.24	44.10	43.98	44.63	58.40	59.53	0.43	30.63	30.42	30.20	30.74	38.83	35.22	36.83
TiO_2	0.61	0.70	1.00	0.61	0.72	n.d.	n.d.	66.12	38.82	38.02	38.37	38.34	3.22	7.17	4.52
Al_2O_3	17.31	13.12	14.05	15.48	14.47	0.85	n.d.	n.d.	1.95	1.88	1.81	1.89	n.d.	n.d.	n.d.
Cr_2O_3	n.d.	n.d.	n.d.	n.d.	n.d.	n.d.	0.02	n.d.	n.d.	n.d.	n.d.	n.d.	n.d.	n.d.	n.d.
FeO	0.80	0.81	0.89	1.01	0.80	1.98	1.72	n.d.	n.d.	n.d.	n.d.	n.d.	1.54	1.64	1.47
MnO	n.d.	n.d.	n.d.	n.d.	n.d.	0.05	0.06	n.d.	n.d.	n.d.	n.d.	n.d.	n.d.	n.d.	n.d.
MgO	27.58	27.17	19.33	19.31	19.39	22.48	23.27	0.54	n.d.	n.d.	n.d.	n.d.	55.06	55.01	55.90
CaO	n.d.	n.d.	13.12	13.34	13.12	12.92	13.06	22.67	28.82	28.39	28.29	29.02	n.d.	n.d.	n.d.
Na_2O	0.48	n.d.	3.20	2.87	3.24	0.23	0.03	n.d.	n.d.	n.d.	n.d.	n.d.	n.a.	n.a.	n.a.
K_2O	10.33	10.62	1.18	1.10	1.11	0.06	n.d.	n.d.	n.d.	n.d.	n.d.	n.d.	n.a.	n.a.	n.a.
F	0.24	0.56	0.63	0.50	0.66	0.32	0.33	0.29	0.39	0.32	0.52	0.23	1.03	1.26	1.02
O-	-0.10	-0.24	-0.27	-0.21	-0.28	-0.13	-0.14	-0.12	-0.16	-0.13	-0.22	-0.10	-0.17	-0.18	-0.16
Total	97.12	93.98	97.23	97.99	97.86	97.16	97.88	89.93	100.45	98.90	98.97	100.12	99.50	100.12	99.58
Si	2.74	2.93	6.26	6.16	6.28	8.01	8.07	0.02	1.00	1.00	1.00	1.00	4.00	2.00	3.00
Ti	0.03	0.04	0.11	0.06	0.08	--	--	1.98	0.95	0.94	0.95	0.94	0.25	0.31	0.28
Al	1.40	1.10	2.35	2.56	2.40	0.14	--	--	0.08	0.07	0.07	0.07	--	--	--
Cr	--	--	--	--	--	--	--	--	--	--	--	--	--	--	--
Fe^{2+}	0.05	0.05	0.07	--	0.06	0.23	0.08	--	--	--	--	--	0.13	0.08	0.10
Fe^{3+}	--	--	0.03	0.16	0.04	--	0.12	--	--	--	--	--	--	--	--
Mn	--	--	--	--	--	0.01	0.01	--	--	--	--	--	--	--	--
Mg	2.83	2.88	4.09	4.03	4.07	4.60	4.70	0.03	--	--	--	--	8.46	4.66	6.79
Ca	--	--	1.99	2.00	1.98	1.90	1.90	0.97	1.00	1.00	1.00	1.01	--	--	--
Na	0.06	--	0.88	0.78	0.88	0.06	0.01	--	--	--	--	--	--	--	--
K	0.91	0.96	0.21	0.20	0.20	0.01	--	--	--	--	--	--	--	--	--
F	0.05	0.13	0.28	0.22	0.29	0.14	0.14	0.02	0.04	0.03	0.05	0.02	0.34	0.23	0.26
SumCat	8.01	7.96	15.99	15.95	15.97	14.95	14.88	3.00	3.02	3.02	3.02	3.03	12.84	7.04	10.17

n.d. = not detected, n.a. = not analysed: amp = amphibole, cho = chondrodite, (c)hu = (clino)humite, ks t= kassite, phl = phlogopite, ttn = titanite

Table 2: Selected electron microprobe analyses of zirconolite, euxenite, thorianite, rutile and geikielite

Mineral	zlt-1	zlt-2	zlt-3	zlt-4	zlt-5	zlt-6	zlt-7	eux	eux-8	tht-9	tht	rt	gk	rt	1σ(ppm)
Na2O	0.02	0.02	0.01	n.d.	n.d.	n.d.	n.d.	0.14	0.31	n.d.	n.d.	n.d.	0.01	0.01	140
FeO	2.37	2.47	3.22	3.07	2.40	2.41	2.43	0.97	0.16	0.04	0.02	0.44	9.36	0.20	96
K2O	0.02	n.d.	n.d.	n.d.	n.d.	n.d.	n.d.	0.20	0.11	n.d.	n.d.	0.01	0.01	0.06	46
ZrO2	30.19	30.53	28.62	29.98	30.68	29.89	30.33	0.05	0.33	0.24	0.31	0.21	n.d.	0.24	251
CaO	11.86	12.63	11.41	11.76	12.75	12.20	12.41	4.47	15.52	0.26	0.06	0.16	0.11	0.05	30
La2O3	0.04	0.03	0.01	n.d.	n.d.	n.d.	n.d.	0.09	0.03	n.d.	0.01	n.d.	n.d.	n.d.	289
TiO2	34.84	36.82	33.09	34.31	37.16	35.94	36.52	28.54	26.42	0.01	n.d.	96.76	63.72	98.33	79
SiO2	0.40	0.48	0.03	0.33	0.37	0.34	0.29	n.d.	n.d.	0.35	0.19	0.21	0.21	0.28	124
Nb2O5	0.76	0.85	1.89	1.32	0.91	0.85	0.87	9.89	1n.d.	n.d.	n.d.	0.04	n.d.	0.03	96
Ce2O3	0.05	n.d.	0.05	n.d.	0.06	0.18	0.03	0.44	0.32	0.10	0.11	0.05	0.02	0.05	248
Ta2O5	0.39	0.20	0.97	0.46	0.36	0.28	0.19	5.85	3.14	n.d.	n.d.	n.d.	n.d.	n.d.	215
Al2O3	0.99	0.92	0.40	0.53	0.88	0.97	1.00	0.08	0.12	0.11	0.16	0.09	0.07	0.07	50
PbO	n.d.	0.02	0.02	0.04	n.d.	n.d.	n.d.	0.10	0.09	0.11	0.31	n.d.	0.01	n.d.	78
Gd2O3	n.d.	0.02	0.06	0.16	n.d.	n.d.	0.03	0.23	n.d.	0.05	n.d.	0.06	n.d.	0.01	299
Pr2O3	0.15	0.01	n.d.	n.d.	0.04	n.d.	n.d.	0.21	0.06	n.d.	n.d.	0.03	n.d.	0.03	324
Y2O3	0.04	0.05	0.05	0.09	0.04	0.04	n.d.	0.16	0.18	0.01	n.d.	n.d.	n.d.	n.d.	114
ThO2	11.35	9.84	13.98	11.67	9.40	10.63	10.15	3.47	3.28	89.61	73.15	n.d.	n.d.	0.01	65
Dy2O3	n.d.	n.d.	0.16	0.22	n.d.	n.d.	0.07	n.d.	n.d.	n.d.	0.10	n.d.	0.01	0.02	305
Nd2O3	0.26	0.11	0.02	0.08	0.08	n.d.	0.11	0.34	0.29	n.d.	0.04	n.d.	0.01	n.d.	292
SrO	0.05	0.06	n.d.	n.d.	0.06	0.08	0.07	n.d.	n.d.	0.02	n.d.	n.d.	n.d.	n.d.	103
Lu2O3	n.d.	n.d.	0.06	0.01	0.07	n.d.	0.07	0.05	0.03	0.07	n.d.	0.01	n.d.	n.d.	177
Sm2O3	0.06	0.12	n.d.	n.d.	n.d.	n.d.	n.d.	0.03	0.03	n.d.	n.d.	0.01	n.d.	n.d.	293
MgO	2.04	1.86	2.00	2.19	1.68	1.83	1.78	0.43	0.36	0.32	0.57	0.74	28.90	0.66	43
MnO	0.05	0.02	0.03	0.06	0.02	0.03	0.01	0.04	n.d.	0.04	n.d.	0.02	0.11	n.d.	99
Ho2O3	0.15	n.d.	0.02	n.d.	0.07	0.15	0.02	0.02	n.d.	0.08	0.02	n.d.	n.d.	0.02	310
Yb2O3	n.d.	n.d.	0.09	n.d.	0.08	0.08	0.04	n.d.	0.01	0.01	n.d.	n.d.	n.d.	0.02	202
HfO2	0.85	0.48	1.50	0.87	1.08	0.81	0.84	n.d.	n.d.	0.10	0.06	0.01	0.12	0.14	167
P2O5	n.d.	0.03	0.02	0.01	n.d.	0.02	0.02	0.05	0.01	n.d.	n.d.	n.d.	n.d.	n.d.	584
UO2	2.82	2.22	1.40	2.13	1.89	2.51	2.31	28.03	26.79	6.18	14.10	n.d.	n.d.	n.d.	72
WO3	n.d.	n.d.	n.d.	n.d.	n.d.	n.d.	n.d.	n.d.	n.d.	n.d.	0.03	0.06	0.01	n.d.	339
Total	**99.76**	**99.79**	**99.12**	**99.30**	**100.06**	**99.25**	**99.61**	**83.87**	**87.58**	**97.69**	**89.23**	**98.92**	**102.68**	**100.23**	

Mineral	zlt-1	zlt-2	zlt-3	zlt-4	zlt-5	zlt-6	zlt-7	eux	eux-8	tht-9	tht	rt	gk	rt
Na	0.002	0.003	0.001	--	--	--	--	0.019	0.036	--	--	--	--	--
Fe	0.125	0.128	0.176	0.164	0.124	0.127	0.127	0.058	0.008	0.002	0.001	0.005	0.236	0.002
K	0.002	--	--	--	--	--	--	0.018	0.009	--	--	--	0.001	0.001
Zr	0.931	0.920	0.910	0.932	0.922	0.917	0.921	0.002	0.010	0.005	0.007	0.001	--	0.002
Ca	0.804	0.836	0.797	0.803	0.842	0.822	0.829	0.341	0.984	0.012	0.003	0.002	0.004	0.001
La	0.001	0.001	--	--	--	--	--	0.002	0.001	--	--	--	--	--
Ti	1.657	1.711	1.622	1.644	1.722	1.699	1.711	1.529	1.176	--	--	0.971	1.446	0.975
Si	0.025	0.030	0.002	0.021	0.023	0.021	0.018	--	--	0.015	0.009	0.003	0.006	0.004
Nb	0.022	0.024	0.056	0.038	0.025	0.024	0.024	0.319	0.268	--	--	0.000	--	0.000
Ce	0.001	--	0.001	--	0.001	0.004	0.001	0.011	0.007	0.002	0.002	--	--	--
Ta	0.007	0.003	0.017	0.008	0.006	0.005	0.003	0.113	0.051	--	--	--	--	--
Al	0.074	0.067	0.031	0.040	0.064	0.072	0.074	0.006	0.008	0.006	0.009	0.001	0.002	0.001
Pb	--	--	--	0.001	--	--	--	0.002	0.001	0.001	0.004	--	--	--
Gd	--	--	0.001	0.003	--	--	0.001	0.005	--	0.001	--	--	--	--
Pr	0.003	--	--	--	0.001	--	--	0.005	0.001	--	--	--	--	--
Y	0.001	0.002	0.002	0.003	0.001	0.001	--	0.006	0.006	--	--	--	--	--
Th	0.163	0.138	0.207	0.169	0.132	0.152	0.144	0.056	0.044	0.873	0.776	--	--	0.000
Dy	--	--	0.004	0.005	--	--	0.001	--	--	--	0.001	--	--	--
Nd	0.006	0.003	--	0.002	0.002	--	0.003	0.009	0.006	--	0.001	--	--	--
Sr	0.002	0.002	--	--	0.002	0.003	0.003	--	--	--	--	--	--	--
Lu	--	--	0.001	--	0.001	--	0.001	0.001	0.001	0.001	--	--	--	--
Sm	0.001	0.003	--	--	--	--	--	0.001	0.001	--	--	--	--	--
Mg	0.192	0.171	0.195	0.208	0.155	0.171	0.165	0.046	0.032	0.020	0.039	0.015	1.300	0.013
Mn	0.003	0.001	0.002	0.003	0.001	0.002	0.001	0.002	--	0.001	--	--	0.003	--
Ho	0.003	--	--	--	0.001	0.003	--	--	--	0.001	--	--	--	--
Yb	--	--	0.002	--	0.001	0.002	0.001	--	--	--	--	--	--	--
Hf	0.015	0.008	0.028	0.016	0.019	0.015	0.015	--	--	0.001	0.001	0.000	0.001	0.001
P	--	0.002	0.001	0.001	--	0.001	0.001	0.003	--	--	--	--	--	--
U	0.040	0.030	0.020	0.030	0.026	0.035	0.032	0.445	0.353	0.059	0.146	--	--	--
W	--	--	--	--	--	--	--	--	--	--	0.000	0.000	0.000	--
Total	**4.081**	**4.082**	**4.077**	**4.091**	**4.072**	**4.076**	**4.076**	**3.000**	**3.000**	**1.000**	**1.000**	**1.000**	**3.000**	**1.000**

n.d. = not detected; zlt = zirconolite, eux = euxenite, tht = thorianite, rt = rutile, gk = geikielite; numbers indicate analysis spots in Fig. 3.